



Seismic Noise-Based Strategies for Emphasizing Recent Tectonic Activity and Local Site Effects: The Ferrara Arc, Northern Italy, Case Study

A. MANTOVANI,^{1,2} N. ABU ZEID,^{1,2} S. BIGNARDI,^{1,2,3} G. TARABUSI,⁴ G. SANTARATO,^{1,2} and R. CAPUTO^{1,2,5} 

Abstract—During the seismic crisis of May–June 2012, that strongly affected the central sector of the Ferrara Arc, relevant coseismic effects were observed, such as ground deformations and amplification phenomena due to low quality mechanical characteristics of the shallow subsurface (i.e. few hundreds of meters). This portion of the subsurface is not investigated by neither hydrocarbon explorations (too deep) nor geotechnical surveys (too shallow). Furthermore, direct analysis is not cost effective to carry out over such a wide area. To overcome these limitations, we exploited seismic noise-based strategies, which are not invasive and do not require expensive equipment. We carried out several single-station and array measurements (i.e. ESAC, Re-Mi, and HVSR), across some of the major tectonic structures of the eastern Po Plain, belonging to the most advanced buried sector of the Northern Apennines. Such investigations were performed along two profiles, about 27 km-long and oriented SSW–NNE, i.e. almost perpendicular to the regional trend of the Ferrara Arc structures. Our results clearly document lateral shear wave velocity variations and the occurrence of resonance phenomena between 0.52 and 0.85 Hz. Additionally, based on inversion procedures, we were able to infer the depth of the resonant interface(s) and we associated such interface(s) to the major known stratigraphic discontinuities, thus emphasizing the recent tectonic activity of the blind thrusts affecting this sector of the Ferrara Arc.

Key words: Seismotectonics, microtremor, ESAC, HVSR, OpenHVSR.

1. Introduction

The Po Plain is one of the most densely populated areas worldwide, because of the favorable combination of morphological, hydrological, climatic factors, and availability of natural resources, which make this, as well as most of the alluvial plains advantageous for the human settlements. Considering the amount of human and infrastructures exposure of the Po Plain associated with its seismogenic potential, it is clear that the seismic risk is particularly high.

The area we investigated pertains to the central-eastern sector of the alluvial Po Plain, which represents the foredeep of two opposite-verging fold-and-thrust belts, the Northern Apennines and the Southern Alps. In particular, we focused on the shallowest portion (down to few hundred meters) of the Ferrara Arc (Fig. 1), which is one of the three major blind arcs, consisting of mainly north-verging thrusts and asymmetric folds forming the external front of the Northern Apennines. Despite its flat topography, past hydrocarbon exploration (Pieri and Groppi 1981) revealed that the external thrusts of the Apennines have fairly irregular shape and are covered by a variable thickness of clastic Pliocene–Quaternary materials (e.g. GeoMol Team 2015).

As it is common in large and tectonically active continental foredeep basins, the Po Plain is characterized by blind faulting (e.g. Vannoli et al. 2014), which became widely debated in the Earth Sciences community in the 80's, when a series of 'hidden earthquakes' hit the central and southern California (1983–1987), and subsequently culminated with the Loma Prieta earthquake in 1989 (Burrato et al. 2012).

Several authors hypothesized that the tectonic activity of the frontal part of the Northern Apennines

¹ Department of Physics and Earth Sciences, Ferrara University, Via Saragat 1, Ferrara, Italy. E-mail: bgnsml@unife.it; rcaputo@unife.it

² Centro Interuniversitario per la ricerca Sismotettonica, CRUST-UniFE, Ferrara, Italy.

³ School of Electrical and Computer Engineering, Georgia Institute of Technology, Georgia, USA.

⁴ Istituto Nazionale di Geofisica e Vulcanologia, Rome, Italy.

⁵ Research and Teaching Center for Earthquake Geology, Thymavos, Greece.

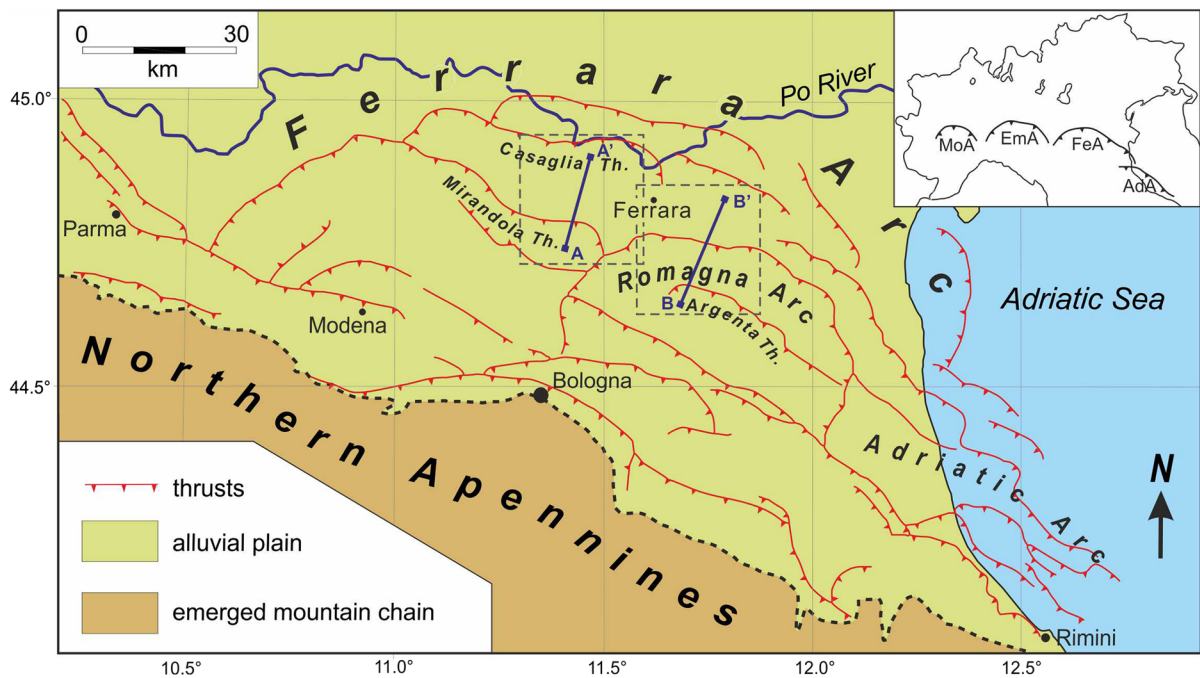


Figure 1

Tectonic sketch map of the Ferrara Arc (after Pieri and Groppi 1981). Dashed boxes delimit the investigated areas (see Fig. 2), while A–A' and B–B' indicate the traces of the two analysed transects. Inset map shows the major tectonic arcs representing the buried external front of the Northern Apennines. *MoA* Monferrato Arc, *EmA* Emilia Arc, *FeA* Ferrara Arc, *AdA* Adriatic Arc

ceased in the early Pleistocene (Argnani and Frugoni 1997; Bertotti et al. 1998; Argnani et al. 2003; Picotti and Pazzaglia 2008); while other studies, based on geomorphological evidence and dynamic inferences, suggested that some of the anticlinal structures buried below the Po Plain may still be tectonically active (Burrato et al. 2003; Boccaletti et al. 2004, 2011; Scrocca et al. 2007).

The latter hypothesis was clearly confirmed by the seismic sequence that affected the eastern sector of the Po Plain on May 20 and 29, 2012 ($M_w = 6.1$ and 5.9, Pondrelli et al. 2012), causing 27 casualties, thousands of injuries, and severe damages, both to historical centers and industrial areas. Besides the relevant social, cultural, emotional and economic impacts, this sequence promoted a new interest about the dynamic properties of the shallow subsurface, especially in connection to the on-going microzoning studies in those areas where site effects were particularly severe (Priolo et al. 2012; Abu Zeid et al. 2012; Caputo and Papathanasiou 2012; Martelli and

Romani 2013; Papathanassiou et al. 2015; Abu Zeid 2016).

Considering the impelling need of characterizing vast areas from the dynamic point of view, the present work focuses on the determination of both the shear-wave velocity distribution and the fundamental resonance frequency of shear waves along two ca. 27 km-long profiles, which perpendicularly cross the tectonic system of the Ferrara Arc (Fig. 2), using passive seismic methods. One major purpose of this research is to improve the knowledge of the geophysical properties of the shallow subsurface in this sector of the Po Plain and particularly their lateral variations that could be captured through the investigation of the propagating wavefields (e.g. Bignardi et al. 2013, 2014). This kind of analyses represent the perfect tool for inferring the recent tectonic evolution of this sector of the Po Plain as recently documented (Tarabusi and Caputo 2016).

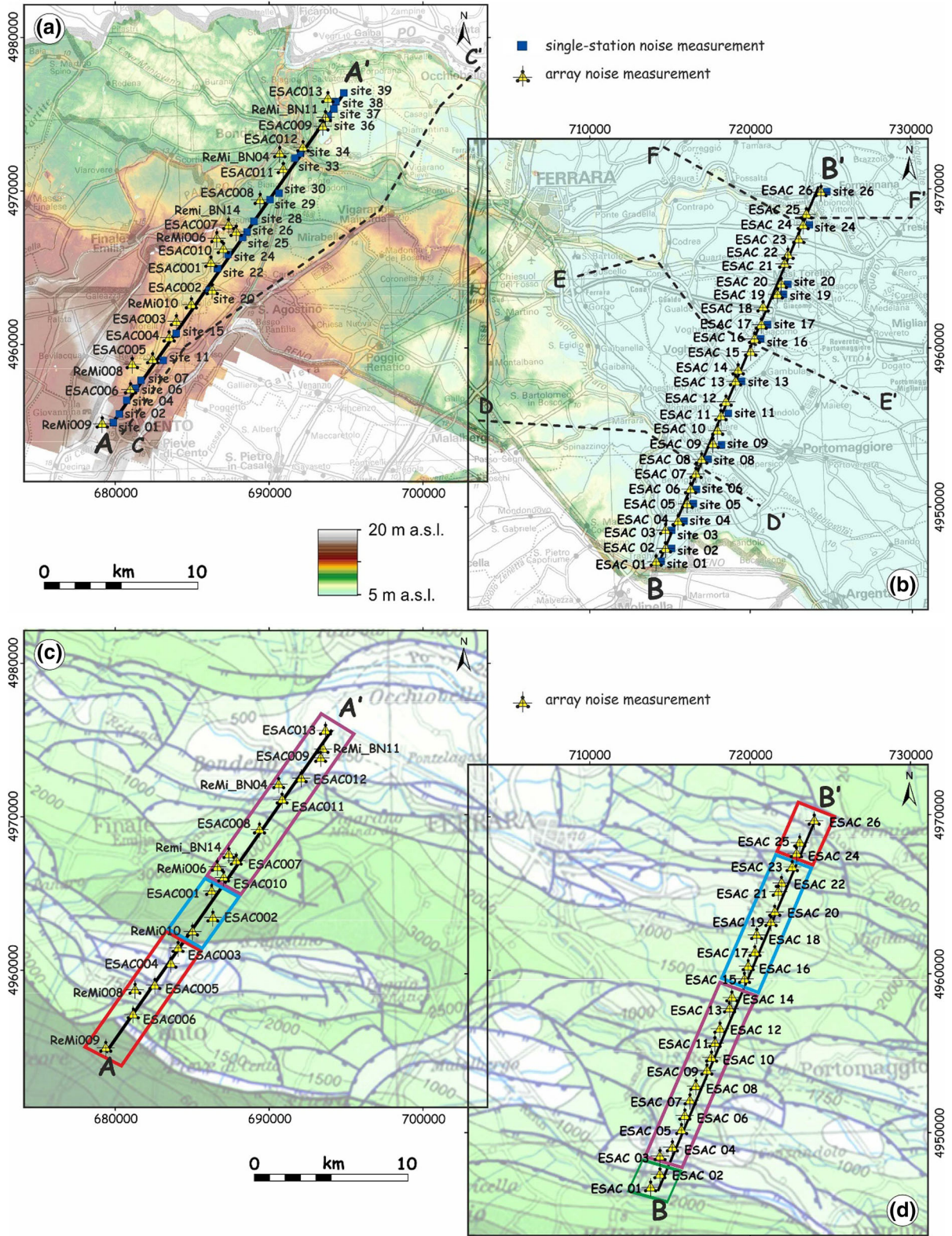
2. *Microzonation and Local Site Effects*

The average shear wave velocity of the shallowest 30 m (v_{s30}), is a widespread parameter for microzonation purposes and site classification in several building codes (Borcherdt 2012). Such a parameter (Borcherdt and Glassmoyer 1992) finds its justification in the studies on the correlation between penetrometric data and seismicity that followed the earthquake of Loma Prieta (California). The limited depth of penetrometric data clearly motivated the limit to the uppermost 30 m. Nowadays, well-defined empirical regression relationships exist to infer the v_{s30} from v_s profiles known to higher depths. If on the one hand the v_{s30} parameter was incorporated in the Italian building code, on the other hand the broader investigated area presents a sedimentary cover whose thickness can even exceed one km. In this geological context, the v_{s30} parameter might reveal insufficient for amplification estimates. Therefore, since the elastic properties of the sedimentary cover play a key role in controlling specific site effects, such as amplification/de-amplification of the seismic-signals, liquefaction, settlement, induced landslides, etc., we decided to extend our investigation beyond the prescribed 30 m (i.e. down to 100–200 m).

The assessment of the regional seismic hazard provides an evaluation of ground shaking for rock or stiff soil conditions (i.e. the so-called seismic bedrock) which can be strongly altered by local effects, both in terms of peak values, duration, and frequency content (Boatwright et al. 1991; Caserta et al. 1999; Margheriti et al. 2000). Such phenomenon was also clearly observed during the May 2012 Emilia seismic sequence (Bordoni et al. 2012).

The need of a reliable strategy for the assessment of the site amplification (i.e. local seismic hazard) led to the development of several techniques capable of identifying the main characteristics of site response due to the presence of soft deposits. The approaches based on numerical simulation coupled with dedicated geophysical and geotechnical surveys (penetrometric tests, cross-hole, borehole, etc.) suffer from severe limitations in urbanized areas because of the elevated cost and site accessibility issues. Alternative techniques use earthquake recordings to experimentally estimate the site response and,

therefore, provide an unbiased estimation of the amplification factor. Although the latter approach is the most reliable, its application is impractical in areas with low seismicity rates (Bonney-Claudet et al. 2006), when rock outcroppings are not available, and/or when bedrock lies at a depth not directly accessible. In general, in the context of site amplification studies a key role is played by the shear-wave velocity (v_s). Indeed, the v_s is directly related to the resistance of subsurface materials to shear forces (Okada 1986; Ohori et al. 2002) and it is therefore important for their quantitative evaluation. Estimating v_s in situ through direct investigation is impractical because of the execution costs and the limited depth of investigation (generally around 30 m). Therefore, the application of low-cost and non-invasive techniques, although indirect, becomes particularly attractive, especially when large areas have to be investigated. Exemplifying comparisons among invasive and non-invasive methods in the Emilian area is discussed in Garofalo et al. (2016a, b). The choice between the most effective investigation method depends on (1) lithology, (2) desired investigation depth, and (3) space available for operating the measurements at the surface. In general, whenever conditions are favourable, geophysical methods provide a faster and low-cost way, as compared to direct methods (Lai et al. 2000). In particular, capturing the distribution of v_s in the subsurface is nowadays possible by leveraging on the dispersive behavior of Rayleigh and Love surface waves recorded by multi-channel recording stations and using low frequency vertical and horizontal geophones respectively. Surface waves methods comprise active (e.g. the Multichannel Analysis of Surface Waves or MASW; Park et al. 1999) and passive approaches. The latter are based on acquisition of the natural seismic noise. In active methods, the investigation depth depends on both the profile length, frequency content and strength of the artificial energy source. Since artificial sources spectra are relatively poor in low frequency (i.e. long wavelengths), the general range of application of active methods, in urban environment, stands for the exploration of the shallow 30–50 m. Differently, natural ambient noise (hereafter ‘noise’), comprises a set of small amplitude oscillations (10^{-4} – 10^{-2} mm)



◀Figure 2

Location of the numerous array and single-station geophysical measurements (yellow triangles and blue squares, respectively) along the two investigated transects. The western profile (A–A'; left maps) runs between the towns of Cento and Bondeno, while the eastern profile (B–B'; right maps) between the towns of Tragheto and Formignana. The background map of **a** and **b** indicates the DTM from LIDAR survey (courtesy of Regione Emilia Romagna, while the dashed lines represent the traces of geological profiles crossing the broader area: C–C' (RER and ENI-Agip 1998); D–D' and E–E' (Molinari et al. 2007); F–F' (ISPRA 2009). The background map of **c** and **d** is from the Structural Model of Italy (Bigi et al. 1992) and it shows the system of mainly reverse faults, all blind, affecting the investigated area; thin contours lines (in meters) and different levels of green indicate the thickness of the Pliocene–Quaternary deposits. Coloured boxes in **c** and **d** indicate relatively homogeneous sectors on the basis of the v_s distribution at depth as shown in Figs. 7a and 8a (see discussion chapter)

of the ground materials characterized by a wide frequency content (0.05–100 Hz), partially below human sensing, originated by a number of different natural sources such as wind, oceanic waves and meteorological conditions (i.e. microseisms) or of artificial origin such as road traffic, trains, and industrial activities (i.e. microtremors; Gutenberg 1958; Asten 1978; Asten and Henstridge 1984). The seismic noise is usually rich in the low frequency range so that passive methods investigation depth mostly depends on the width of the geophone array.

Indeed, since the pioneer work of Kanai et al. (1954), the seismic ambient noise became a widely used tool for the estimation of the seismic site response and for inferring the dynamic properties of the subsurface, especially when incoherent sediments are present. In order to gain insight on the shear wave velocity variation in the shallow subsurface as well as on the fundamental resonance frequency of sediments, we used natural seismic noise-based methods, namely: the Extended Spatial AutoCorrelation (ESAC; Ohori et al. 2002; Okada 2003), the Refraction Microtremors (Re-Mi; Louie 2001) and the Horizontal to Vertical Spectral Ratio, or HVSR (Nogoshi and Igarashi 1970; Nakamura 1989), at sparse locations across the area, so to cover the entire territory under investigation.

In particular, we systematically collected data regularly spaced along the two above mentioned transects (Fig. 2) with the aim of reconstructing pseudo-2D sections of the shallow sedimentary cover,

down to 160 m. This strategy (explained in more detail in a following section of the paper) allowed us to emphasize the occurrence of lateral variations of the shear wave velocity and the fundamental frequency, which reflect analogous stratigraphic changes. In order to investigate also the presence of deep discontinuities in terms of major elastic impedance contrast, the obtained shear wave velocity profiles have been used as input start models for the inversion of the HVSr curves.

3. Geological and Geodynamic Framework of the Po Plain

The Po Plain represents the widest nearly flat area of Italy, extending for over 400 km in an approximately E–W direction from the western Alps to the Adriatic Sea, and it corresponds to the drainage basin of the Po River and its tributaries. Its morphological boundaries are represented by the contact between the Quaternary alluvium outcropping in the plain, the Southern Alps to the north and the exposed portion of the Northern Apennines to the south.

The structural setting of the Po Plain was imaged for the first time during the past decades by a dense grid of reflection seismic profiles in the frame of hydrocarbon and water resources explorations (AGIP-mineraria 1959; AQUATER 1976, 1978; AQUATER-ENEL 1981). The most impressive features of the Po Plain are buried beneath a thick syntectonic succession, deposited in the Neogene–Quaternary foredeep (Fig. 1). This configuration is the result of fast subsidence–sedimentary rates and low tectonic activity. The combined action of these opposing mechanisms resulted in the complete sealing of the external fronts of the Northern Apennines. Actually, the real front of the fold-and-thrust belt is located in the central-southern portion of the Po Plain and comprises four major blind arcs: the Monferrato Arc, the Emilia Arc, the Ferrara Arc and the Adriatic Arc (Castellarin et al. 1985; see inset map in Fig. 1). In particular, the Ferrara Arc started to develop in Early Pliocene (Costa 2003; AQUATER 1978, 1980; in Middle-Late Pliocene, according to Patacca and Scandone 1989), nowadays it runs from Reggio Emilia town to the Adriatic Sea and consists of

Messinian-Quaternary autochthonous and parautochthonous, terrigenous deposits overlying Mesozoic to Palaeogene carbonate units (Pieri and Groppi 1981; Nardon et al. 1991; Masetti et al. 2012). The outer border of this arc is marked by a set of structural highs originated by fault-propagation folds arranged roughly en-echelon (e.g. Pieri and Groppi 1981), where the thickness of the Quaternary succession is locally only 100 m or less (Paolucci et al. 2015; Tarabusi and Caputo 2016). In contrast, the inner and outer portions of the arc are depressed and covered by a Quaternary sequence locally thicker than 800 m.

The architecture of the Po Plain foredeep infilling, from Pleistocene onward, is characterized by a generally regressive trend, interrupted by smaller fluctuations, evidenced by the transition from offshore Pliocene deposits to marine-marginal and then to alluvial Quaternary sediments (Lucchi 1986; Amorosi and Colalongo 2005; Amorosi 2008).

The great number of subsurface data collected during hydrocarbon explorations and water research (AGIP-MINERARIA 1959; AQUATER 1976, 1978; AQUATER-ENEL 1981; Pieri and Groppi 1981; RER and ENI-AGIP 1998; Boccaletti et al. 2004, 2011; Molinari et al. 2007) allowed to map the main Quaternary unconformities as well; at the regional scale the most recent of such surfaces represents the base of the Upper Emiliano-Romagnolo Synthem (AES; Boccaletti et al. 2004) which consists of a series of different depositional cycles whose limits are placed in correspondence of the bottom of the transgressive marine deposits. The transgressive portion of each cycle is characterized by the presence of fine materials (e.g. floodplain, marsh and coastal plain clays) with subordinated sandy intercalations. Instead, the regressive sequence consists of alluvial plain deposits (e.g. fine sediments of overflowing river) where channel sands are subordinated in the form of isolated lenticular bodies. On top of each cycle, the channel sands become abundant, thus forming laterally wider bodies (RER and ENI-AGIP 1998; ISPRA 2009).

Several studies reveal that the Quaternary succession is highly deformed and confirm that the transitions from marine to continental sediments coincide with important tectonic phases followed by periods of strong subsidence (RER and ENI-AGIP

1998; Boccaletti et al. 2004, 2011; Abu-Zeid et al. 2013, 2014; Martelli and Romani 2013; Molinari et al. 2007; Paolucci et al. 2015; Tarabusi and Caputo 2016). Therefore, the highly variable thickness of the Quaternary sequence, from several hundreds of meters in the synclines to few tens of meters in correspondence of the growing anticlines, like those named Mirandola, Casaglia, and Argenta (Fig. 1), reflects the influence of the complex evolution of the blind thrusts belonging to the major Ferrara Arc.

4. Geophysical Noise-Based Methods

In order to reconstruct the geophysical pseudo-2D sections along the two transects, three different geophysical methods were employed, viz. Re-Mi, ESAC, and HVSR. These methods share the use of natural seismic noise as a probe of the elastic properties of the subsurface, which in turn, is conceptualized as a stack of parallel layers (i.e. the subsurface is assumed 1D). As such, the pseudo-2D section is obtained as the interpolation of locally 1D models. ESAC and Re-Mi techniques pertain to the array methods, in which an array of geophones is deployed on the investigated area.

4.1. Re-Mi Method

The Re-Mi method implements a linear array and presents minimal differences compared to its active-source analogous MASW. The recorded seismogram (originally in time-offset representation) is translated into the spectral domain using a procedure similar to the two dimensional Fourier transform (often referred as *f-k* transform; Capon 1969). While in MASW the *f-k* domain is preferably translated to the frequency-velocity representation, the processing of seismic noise is typically achieved by the use of the “*p-tau*” (slowness-intercept; Thorson and Claerbout 1985) or the “*p-f*” transform (slowness-frequency; McMechan and Yedlin 1981). If the wavefield is dominated by surface waves, in this new bi-dimensional representation the spectral maxima are arranged according the dispersive behavior of surface waves and dispersion curves can be extracted by means the “picking” operation. The spectral transforms mentioned above

implicitly assume that waves propagate parallel to the array and therefore their velocity (at each frequency) depends on the travel-time from one receiver to the next. In MASW the assumption is exact and the dispersion curve is extracted by locating the spectral maxima. Differently in Re-Mi, where the recorded surface waves ideally possess isotropic arrival directions, this basic assumption is broken. In particular, those waves with non-parallel propagation direction (i.e. the majority) will possess an augmented apparent velocity. To retrieve true velocities, Louie (2001) proposed that the dispersion curve should be picked at the interface zone where dispersion waves energy starts to show appreciable amplitude. Small black boxes in Fig. 3a are based on the application of such technique for site Re-Mi_BN11, along transect A–A'. Based on this approach, dispersion curves obtained from the analysis of the measured noise data at selected locations using the Re-Mi technique are shown in Fig. 4a. Finally, the 1D subsurface model that best reproduces the dispersion curve is estimated through an inversion process.

4.2. ESAC Method

ESAC is a variant of the original Spatial Auto-Correlation (SPAC; Aki 1957, 1964). While SPAC is limited to the use of circular arrays with an additional receiver in the center, ESAC is designed in such a way that X-, L- or T-shaped arrays can be employed. The mathematical basis of the two methods is very similar and a detailed derivation can be found in (Aki 1957, 1964; Ohori et al. 2002). Typically, in SPAC the normalized cross spectrum S_{AB} of the signals recorded at a receiver pairs, A and B, is computed, where A is the receiver at the center of the circular array. The azimuthally averaged spatial autocorrelation function $S(f,r)$ of frequency f and receivers separation r , is computed as the average of the real part of all S_{AB} (summing over all B receivers on the circle). The apparent phase velocity $c(f)$ satisfies the following analytical equation:

$$S(f,r) = J_0 \cdot [2 \cdot \pi \cdot f \cdot r / c(f)] \quad (1)$$

where J_0 is the zero-th order Bessel's function.

The phase velocity $c(f)$ can then be obtained by fitting the azimuthally averaged spatial autocorrelation

function to the afore-mentioned Bessel function. In determining $c(f)$ from Eq. (1) one might either keep constant r or f . In SPAC method r is held constant, while the ESAC method is obtained by using the constant f condition. This latter choice has the advantage of relaxing the constraint on the shape of the array. Finally, the phase velocity $c(f)$ is inverted to retrieve the velocity in the subsurface. Similar to Re-Mi, the dispersion curve was calculated using the p-tau transform which implies the use of all receivers taking into account their relative position (Figs. 3b, 4b).

4.3. HVSR Method

Differently from array approaches, the HVSR method implements a single station capable of simultaneously recording the three components of motion (often in form of velocity). Such a technique has become increasingly popular and its application spans a variety of scientific disciplines, such as geology (Tarabusi and Caputo 2016; Mantovani et al. 2018), seismology and microzonation studies (Scherbaum et al. 2003; Gallipoli et al. 2004; Albarello et al., 2011; Massolino et al. 2018) and even archaeology (Obradovic et al. 2015; Abu Zeid et al. 2016, 2017). One of the most attractive aspects of the method is the possibility of estimating the elastic properties of the subsurface, and in particular, the depth of the major impedance contrasts (i.e. in most cases the depth of the bedrock) through dedicated processing and inversion procedures (see Bignardi 2017, for more details). The availability of fast and efficient modelling strategies favored the implementation of algorithms for the inversion of such curves, for example the commercial software Grilla[®] (<http://www.moho.world>) or the open source Geopsy (<http://geopsy.org>). Recently, Herak (2008) published a user friendly program in Matlab capable of obtaining the 1D distribution of the elastic properties of a subsurface consisting of a stack of layers by inverting a single HVSR curve, and later, Bignardi et al. (2016, 2018a, b) published a set of programs dedicated to the processing and inversion of sparsely distributed microtremor measurements (<https://github.com/sedysen/OpenHVSR>).

The geophysical information is extracted by the comparison between horizontal and vertical

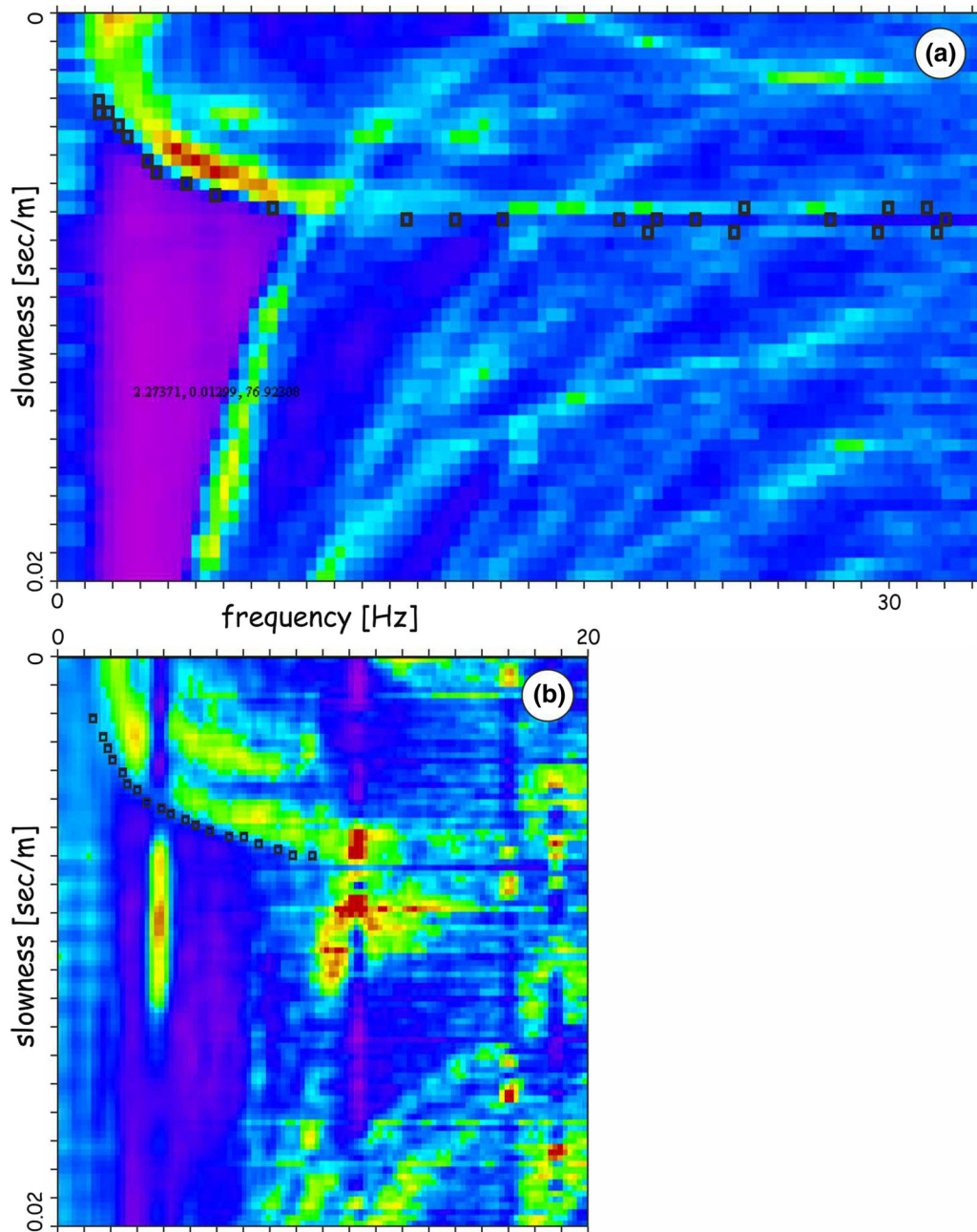


Figure 3

Examples of dispersion images processed from 24-channel linear array using the slowness-frequency (p-f) technique from sites Re-Mi_BN11 (a) and ESAC009 (b), both along the western A–A' transect (see Fig. 2a for locations). Colours refer to the normalized spectral ratio with respect to the average power of all recordings for the specific site. Black squares indicate the position of the manually picked points based on the approach proposed by Louie (2001) providing the dispersion curve

components of the wavefield which is embodied in the so called “HVSr curve”. Typically, the three components of motion are split into several time

windows of pre-defined length. For each data window the Fourier spectra of all components are computed and properly smoothed. Horizontal components are

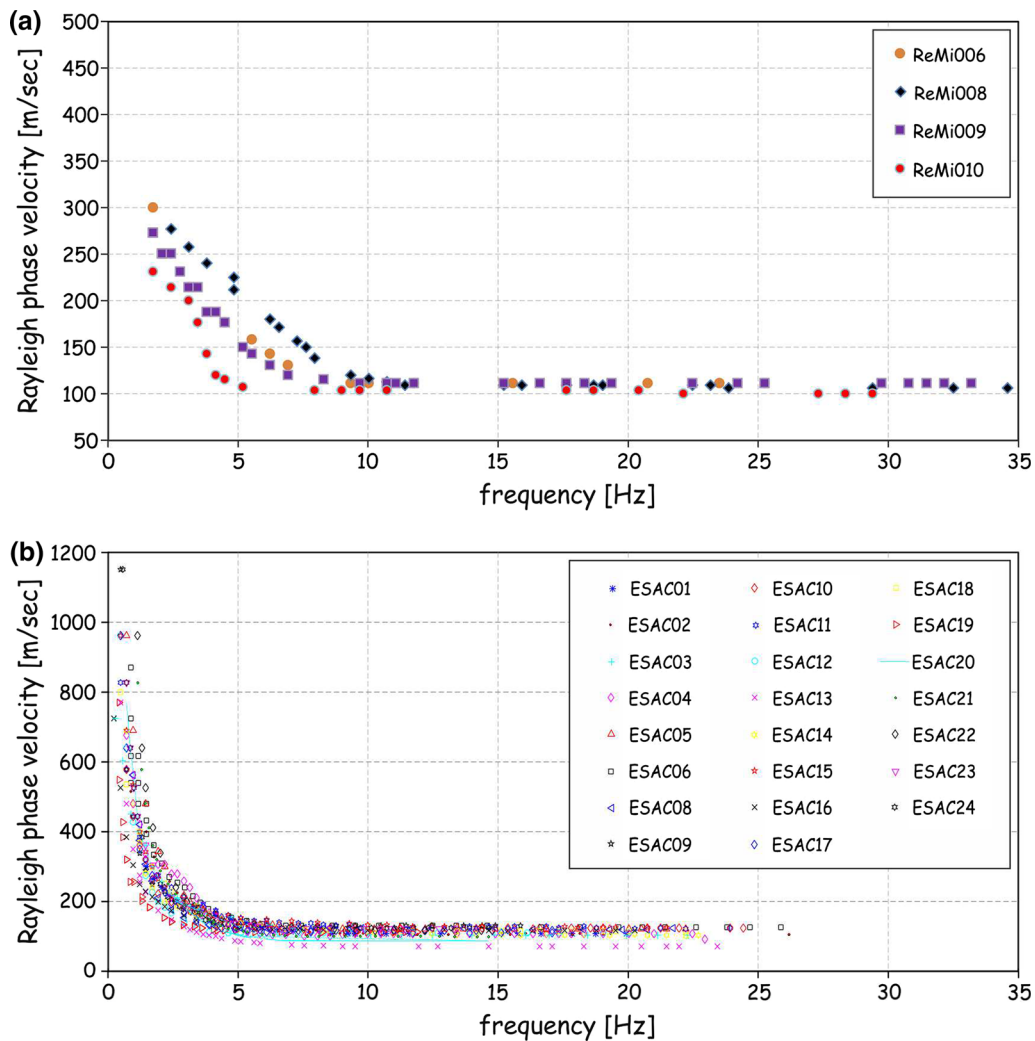
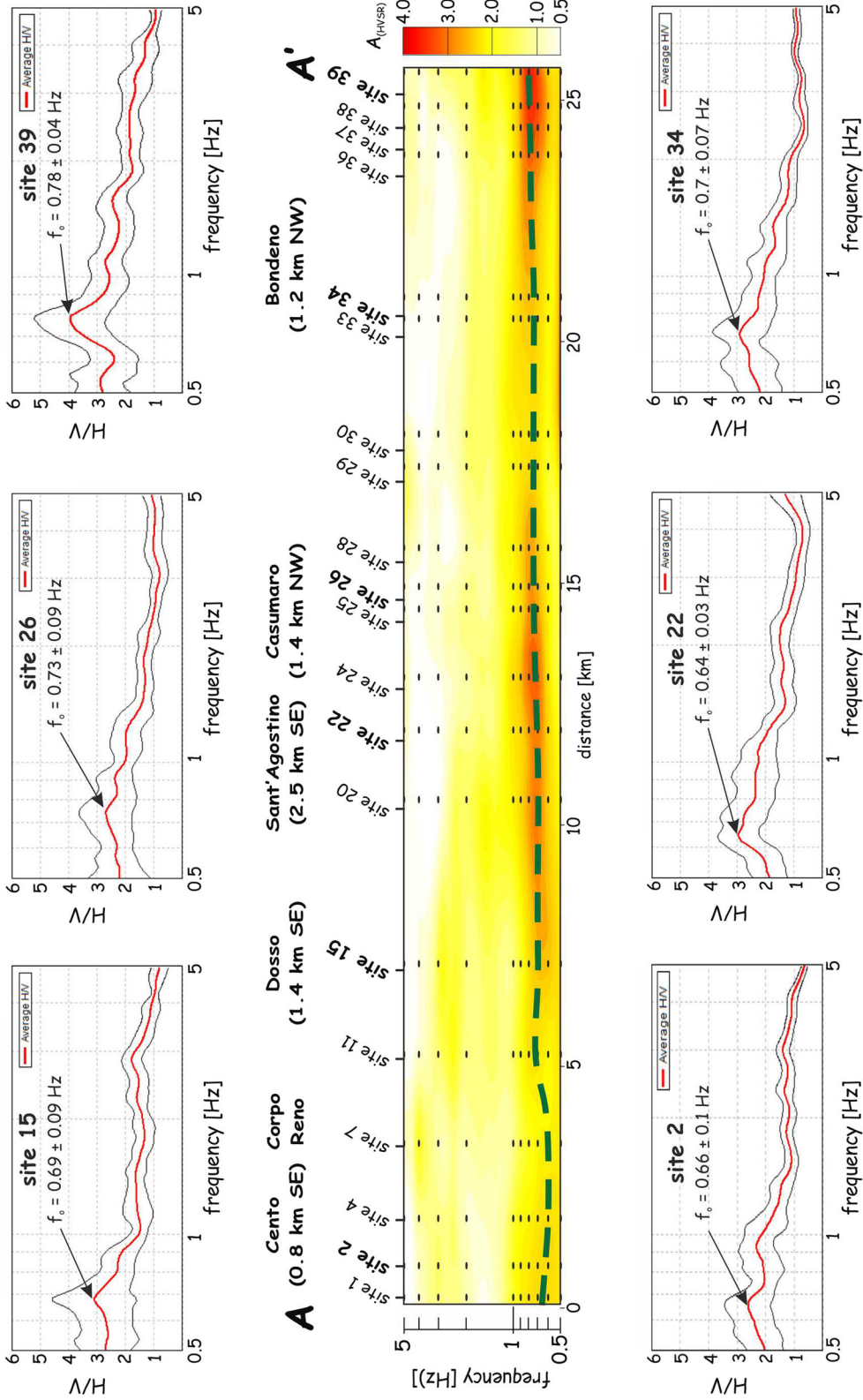


Figure 4

a Examples of dispersion curves processed from 24-channel linear arrays using the slowness-frequency (p-f) technique for selected sites along A–A' transect measured with the Re-Mi technique. **b** Dispersion curves for most sites along B–B' transect obtained processing the seismic noise using the ESAC method. All curves show the good quality level of the processed data

combined to obtain the total horizontal amplitude and finally, the HVSR curve is obtained as the ratio between the average horizontal over the vertical spectra. When the subsurface can be considered locally consisting of a stack of sedimentary layers residing on a hard bedrock, the curve will exhibit one or more peaks directly connected with major increases (with depth) in elastic properties. Despite the fact that several elastic parameters come into play in shaping the curve, each to a different degree (Tarabusi and Caputo 2016), a central contribution is

provided by thickness and v_s of the layers. The general appearance of the curve also depends on the nature of the recorded wavefield (i.e. body v_s surface waves, distribution of natural sources) (Bonneyfoy-Claudet et al. 2006; Lunedei and Albarello 2015; Matsushima et al. 2014), as well as site local effects (Martorana et al. 2018), and some subjectivity in the processing (D'Alessandro et al. 2016). Ultimately however, regardless of the nature of the wavefield, it is quite established that the local maxima of the curve coincide with the resonance frequency(ies) of the



◀Figure 5

Smoothed 2D HVSR profile produced by interpolating the average HVSR curves (frequency range 0.5–5 Hz) for the western transect (A–A'). Relative amplitudes are colour-coded (see the colour bar on the electronic version of this paper). The lateral evolution of the main peak (f_0) along the interpolated profile is highlighted by the dashed green line. Examples of HVSR curves are provided for selected locations

shear body waves (Albarelo and Castellaro 2011). Examples of HVSR curves are shown in Fig. 5. Details on the procedure and criteria for the evaluation of the quality of such curves can be found in Bard (1999) and SESAME (2004). Once the HVSR curve is obtained, the model capable of best reproducing it is estimated through a Monte Carlo approach.

4.4. HVSR-Guided Inversion

In order to improve our understanding of the subsurface, all the HVSR curves were also inverted using the OpenHVSR software (Bignardi et al. 2016), which features the same modeling routines of ModelHVSR (Herak 2008). It is based on the Tsai and Housner (1970) approach for the body waves propagation, and the routine from Lunedei and Albarelo (2010) to account for surface waves and it is implemented in a way that makes data management much more flexible thus reducing computational times.

During the search for the subsurface model at each investigated site, which best reproduces the experimental HVSR, a large range of the visco-elastic parameters is investigated through the Monte Carlo method (Bignardi et al. 2016). The parameters space exploration is optimized by considering an initial model and then investigating random perturbations of its parameters. A real valued functional, often referred to as “energy”, which evaluates the fit between the experimental and simulated curves is built and used to evaluate the performance of each perturbed model. The lower is the energy, the better is the fit, and in turn, the better the model will reproduce the experimental curve. In the present study, the subsurface with the best performances according to both the afore-

mentioned modeling routines (i.e. ModelHVSR and OpenHVSR) was sought. In the process, every time that a model with lower energy is found, it is recognized as new best model and henceforth used as a reference subsurface from which perturbations are produced. If such a strategy delivers very good computational performances and it is robust in avoiding local energy minima, on the other hand, the user is required to provide an initial model to start from. In our study, the input model, in terms of v_p and v_s , was provided by the output of the ESAC method (see previous section). In this way, we obtained the advantage of starting from a model capable of reproducing the dispersion curves of surface waves and likely to reside in the “basin attraction” of the HVSR inversion global minima. Nevertheless, ESAC and HVSR inversion processes are based on forward models with inherently different simulation approaches. While the ESAC inversion is engineered to produce a smooth model comprising a large number of layers, inversion of HVSR curves requires few clear velocity contrasts and few layers are in general sufficient as a start model. As such, the ESAC output is not optimal as initial model for the HVSR inversion. Following these considerations, the smooth v_s subsurface model obtained from the ESAC was piecewise averaged to produce a blocky layered model to be used as a starting guess to initiate the HVSR inversion process (Fig. 6a). Knowing v_s in the profile, the piecewise averaged stack of layers was determined such that the average shear wave velocity and total depth computed from the surface down to the bottom of the layer “L”, indicated with v_{sL} and H_L respectively, would roughly fulfill the following equation

$$f_L = v_{sL}/4 \cdot H_L \quad (2)$$

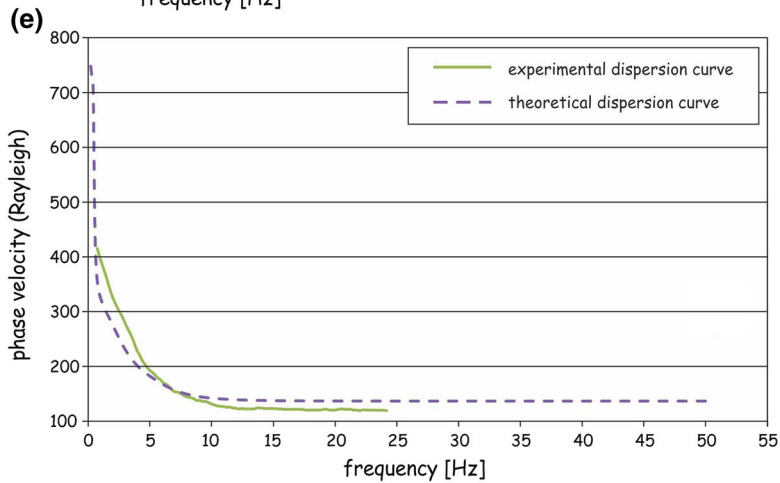
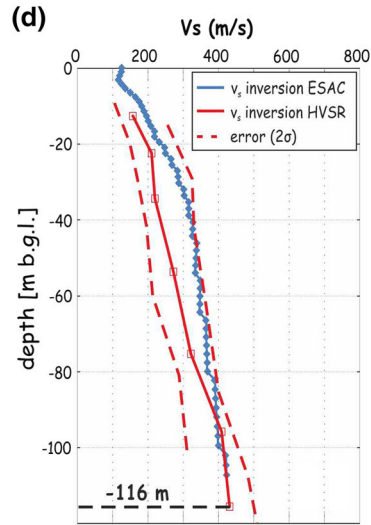
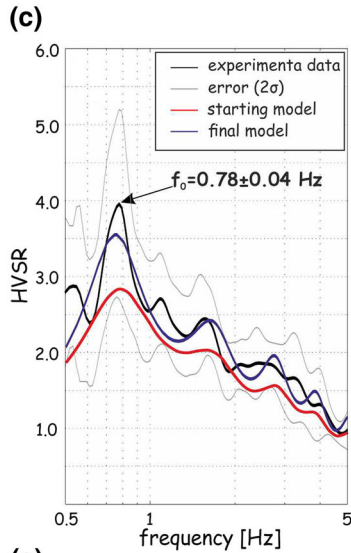
where f_L are the frequency locations of the observed peaks of the curve. Subsequently, and when necessary according to expert judgment and extensive testing, the layers were split into a variable number of sublayers to provide additional degrees of freedom. The piecewise average v_p values were obtained by averaging the v_p from ESAC according to the same depth partitions obtained for the v_s , while for the density and attenuation factors, the values suggested by Laurenzano et al. (2013) were used. This strategy was repeated for each measured site, obtaining a set

(a) **starting model**

Vp [m/s]	Vs [m/s]	ρ [g/cm]	thickness [m]	Qp	Qs
1466.0	143.0	1.5	10.1	20.0	10.0
1543.0	211.0	1.5	9.4	40.0	10.0
1601.0	271.0	1.8	10.8	40.0	20.0
1650.0	324.0	1.9	19.7	40.0	20.0
1688.0	352.0	1.9	20.8	40.0	20.0
1715.0	382.0	1.9	21.1	40.0	20.0
1736.0	413.0	2.0	18.0	45.0	25.0
2000.0	800.0	2.1	999.0	999.0	999.0

(b) **final model**

Vp [m/s]	Vs [m/s]	ρ [g/cm]	thickness [m]	Qp	Qs
1456.2	159.9	1.5	12.7	8.4	5.0
1532.3	212.8	1.5	9.9	9.3	5.0
1628.2	222.2	1.7	12.1	8.3	5.0
1639.9	274.3	1.8	19.4	30.8	19.4
1697.6	324.0	2.0	21.9	36.9	15.7
1740.9	410.7	2.0	20.7	40.2	24.3
1776.9	433.4	2.1	19.9	32.6	16.5
2000.0	600.0	2.1	999.0	999.0	999.0



◀Figure 6

Example of HVSR processing and inversion (site 39 along the western profile A–A') with OpenHVSR routine (Bignardi et al. 2016). **a** Starting subsurface blocky layered velocity model obtained by piecewise averaging the smooth subsurface obtained from ESAC inversion. **b** Final subsurface velocity model based on the inversion of the HVSR curve (see text for details on procedure). **c** Comparison between HVSR curves from experimental data (black line) and those simulated based on the starting (red) and final (blue) velocity models. **d** Comparison between the smooth v_s model obtained from the closest ESAC site (blue line) and the final blocky model obtained after HVSR inversion (red lines, with 2σ curves dashed). **e** Comparison between theoretical dispersion curve calculated for the final subsurface velocity model and the corresponding experimental dispersion curve

of very good starting models. In order to perform the optimization of the subsurface and to reproduce the HVSR peaks a maximum perturbation of 5% of the elastic parameter (i.e. v_p , v_s , thickness, density, P-wave and S-wave frequency-dependent attenuation) was allowed for the first 5000 model generations, and successively, in order to enrich the space of parameters sampling, a 15% perturbation was allowed for the subsequent 25,000 runs. In the process, the visco-elastic parameters of the half-space, were kept fixed.

5. Data Collection and Processing

With the purpose of investigating the presence of strong lithological lateral variations (in terms of elastic properties), two transects were selected almost perpendicular to the regional trend of the buried structures belonging to the Ferrara Arc, and oriented SSW–NNE. Both profiles, ca. 27 km-long, were investigated by means of numerous noise acquisitions both in array and as single-station.

Along the western profile (A–A'; Fig. 2a), extending from the town of Cento to the town of Bondeno, 7 Re-Mi, 13 ESAC, and 21 HVSR measurements were performed starting from early 2012 to May 2015.

The investigation of the second profile, performed mostly in 2014–2015 (B–B'; Fig. 2b), extended from the village of Traghetto to the village of Formignana and consisted in 26 ESAC (Abu-Zeid et al. 2013, 2014) and 16 HVSR.

ESAC and Re-Mi acquisitions were performed with an average spatial sampling of about 1 km, while HVSR sampling was around 1.2 km for the western transect and 1.6 km for the eastern one (Fig. 2a, b). Further details regarding ESAC and Re-Mi measurements for the western and eastern profiles are summarized in Tables 1 and 2, respectively, while details regarding HVSR measurements can be found in Tables 3 and 4.

ESAC measurements were acquired using an in-house built digital seismograph. An L-shaped array, comprising 24 three-component low frequency geophones (4.5 Hz), 8 m-spaced, was deployed at each site. The resulting mean array aperture of about 130 m allowed to confidently investigate the subsurface down to 160 m depth. Seismograms ranging between 5 and 15 min were continuously recorded at 500 Hz sampling frequency and processed using the software SeisImager (2009).

Re-Mi profiles were acquired using 24 vertical geophones (4.5 Hz natural frequency) and 8 m-spaced connected to a RAS-24 digital seismograph (Seistronix, USA). Multiple recordings (32 ms-long) were performed with a sampling frequency of 500 Hz and processed using the SeisOpt^R ReMiTM Software (<http://www.optimsoftware.com/index.php/seisopt-remi-byoptim-software>).

Finally, the single-station noise measurements were performed using a three-component short-period seismometer, with 2 Hz proper frequency, connected to a portable seismograph (Vibratlog model, MAE srl, Italy, <http://www.mae-srl.it>). Such an instrument can comfortably retrieve the spectral ratio down to 0.1 Hz and thus investigate depths that may potentially exceed one km (see, e.g., Mulargia and Castellaro 2016). Following the SESAME Guidelines (SESAME 2004) and since the resonance frequency was expected below 1 Hz, the shortest acquisition time was 30 min, at 250 Hz sampling rate. The seismometer was placed in a small hole filled with sand to ensure easy levelling, good coupling with the ground and prevent any turbulence from wind flowing around the seismometer (SESAME 2004; Mucciarelli et al. 2005). Seismograms were processed using the Grilla[®] software (<http://www.moho.world>) and results are summarized in Tables 3 and 4, respectively (columns f_0 and A_0).

Table 1

List of the array noise measurements along the Cento-Bondeno A–A' transect (see Fig. 2a)

Label	x	y	Elevation (m asl)	Distance (m) along A–A'	Distance (m) to A–A'
ReMi009	4,955,137	680060	14.5	50	25
ESAC006	4,957,327	681,804	13.0	2845	195
ReMi008	4,958,886	681,953	11.3	4207	577
ESAC005	4,959,220	683,215	12.6	5205	264
ESAC004	4,960,593	684,254	12.6	6925	326
ESAC003	4,961,670	684,477	12.5	7935	110
ReMi010	4,962,672	685,739	11.9	9480	348
ESAC002	4,963,563	687,038	12.0	10,956	900
ESAC001	4,965,344	686,964	11.1	12,371	183
ESAC010	4,966,198	687,706	10.0	13,496	66
ReMi006	4,966,903	687,298	10.4	13,839	805
ESAC007	4,967,237	688,560	10.3	14,837	36
ReMi_BN14	4,967,683	688,077	10.7	14,925	615
ESAC008	4,969,316	690,045	8.9	17,392	58
ESAC011	4,971,209	691,492	7.7	19,773	155
ReMi_BN04	4,972,286	691,344	8.7	20,570	583
ESAC012	4,972,657	692,754	8.2	21,683	357
ESAC009	4,973,993	694,016	7.6	23,502	623
ReMi_BN11	4,974,513	694,165	8.1	24,013	447
ESAC013	4,975,738	694,350	7.1	25,122	104

Coordinate values refer to UTM zone 32 N, WGS84

Table 2

List of the array noise measurements along the Traghetti-Formignana B–B' transect (see Fig. 2b)

Label	x	y	Elevation (m asl)	Distance (m) along B–B'	Distance (m) to B–B'
ESAC 01	4,946,530	714,459	3.1	0	178
ESAC 02	4,947,330	715,029	2.3	831	44
ESAC 03	4,948,470	715,036	1.2	1883	483
ESAC 04	4,949,020	715,811	1.3	2692	15
ESAC 05	4,950,090	716,382	1.5	3900	122
ESAC 06	4,950,990	716,572	0.5	4803	55
ESAC 07	4,951,940	716,901	1.3	5805	123
ESAC 08	4,952,830	717,258	1.2	6764	143
ESAC 09	4,953,800	717,964	1.3	7933	127
ESAC 10	4,954,610	718,249	3.9	8790	73
ESAC 11	4,955,510	718,460	3.2	9700	84
ESAC 12	4,956,410	718,774	4.4	10,652	147
ESAC 13	4,957,680	719,364	3.5	12,052	100
ESAC 14	4,958,360	719,532	2.0	12,743	212
ESAC 15	4,959,510	720,312	0.2	14,107	56
ESAC 16	4,960,300	720,546	0.2	14,925	37
ESAC 17	4,961,180	720,964	0.9	15,898	3
ESAC 18	4,962,270	721,064	2.8	16,941	330
ESAC 19	4,963,050	721,965	1.5	18,011	193
ESAC 20	4,963,680	722,199	0.9	18,682	163
ESAC 21	4,964,950	722,408	0.5	19,933	141
ESAC 22	4,965,510	722,620	0.2	20,531	165
ESAC 23	4,966,480	723,283	1.9	21,683	66
ESAC 24	4,967,330	723,543	2.4	22,567	27
ESAC 25	4,968,010	723,757	3.6	23,277	96
ESAC 26	4,969,390	724,651	2.2	24,897	187

Coordinate values refer to UTM zone 32 N, WGS84

Table 3

List of the single-station noise measurements along the Cento-Bondeno A–A' transect (see Fig. 2a)

Label	x	y	Elevation (m asl)	Distance (m) along A–A' (m)	Distance (m) to A–A' (m)	f_0 (Hz)	A_0	v_s (m/s)	Inferred elevation (m bsl)
Site 01	4,955,190	680,079	14.8	105	10	0.63 ± 0.08	2.5	280	96
Site 02	4,955,730	680,459	13.6	765	11	0.66 ± 0.09	2.6	272	95
Site 04	4,956,600	680,921	12.5	1742	110	0.58 ± 0.07	2.6	301	146
Site 06	4,957,360	681,481	14.0	2686	87	0.52 ± 0.03	3.1	295	138
Site 07	4,957,870	681,826	12.9	3302	98	0.60 ± 0.01	2.4	313	123
Site 11	4,959,140	683,232	12.3	5149	323	0.79 ± 0.04	2.8	330	107
Site 15	4,960,850	684,062	11.7	7026	21	0.69 ± 0.09	3.1	299	113
Site 20	4,963,560	686,137	11.1	10,436	164	0.64 ± 0.03	3.1	237	98
Site 22	4,964,940	686,688	11.2	11,882	177	0.64 ± 0.03	2.9	242	103
Site 24	4,965,810	687,340	10.2	12,969	143	0.75 ± 0.16	3.5	292	104
Site 25	4,966,888	688,273	11.2	14,387	2	0.73 ± 0.05	2.7	319	111
Site 26	4,967,260	688,551	10.0	14,851	15	0.73 ± 0.09	2.7	321	112
Site 28	4,967,920	689,000	9.3	15,649	4	0.73 ± 0.05	3.0	320	115
Site 29	4,969,300	690,001	9.0	17,354	31	0.67 ± 0.16	2.5	348	122
Site 30	4,969,700	690,579	7.8	18,013	275	0.66 ± 0.05	2.8	310	119
Site 33	4,971,930	691,579	8.5	20,413	187	0.66 ± 0.04	2.9	292	102
Site 34	4,972,230	691,921	11.5	20,855	80	0.70 ± 0.07	2.9	302	102
Site 36	4,974,600	693,686	8.3	23,809	5	0.76 ± 0.08	3.5	304	116
Site 37	4,975,040	694,046	6.5	24,376	47	0.72 ± 0.06	3.8	278	114
Site 38	4,975,510	694,174	7.2	24,834	118	0.73 ± 0.11	3.7	279	113
Site 39	4,976,030	694,673	6.1	25,547	8	0.78 ± 0.04	4.0	281	117

Coordinate values (x, y) refer to UTM zone 32 N, WGS84. All measurements lasted 30 min

 f_0 peak frequency, A_0 HVSR amplitude at peak frequency, v_s average velocity above principal resonant surface

Table 4

List of the single-station noise measurements along the Traghetti-Formignana B–B' transect (see Fig. 2b)

Label	x	y	Elevation (m asl)	Distance (m) along B–B'	Distance (m) to B–B'	f_0 (Hz)	A_0	v_s (m/s)	Inferred elevation (m bsl)
Site 01	4,946,660	714,455	2.5	0	314	0.79 ± 0.04	2.4	274	92
Site 02	4,947,420	715,103	2.5	937	16	0.84 ± 0.29	2.3	273	84
Site 03	4,948,550	715,112	1.1	2013	451	0.82 ± 0.02	2.4	288	82
Site 04	4,949,120	715,877	1.5	2805	31	0.82 ± 0.01	3.1	232	80
Site 05	4,950,220	716,457	1.5	4037	137	0.85 ± 0.09	2.3	261	78
Site 06	4,951,100	716,648	0.9	4928	32	0.66 ± 0.08	2.7	359	172
Site 08	4,952,950	717,359	1.0	6905	102	0.70 ± 0.06	2.1	278	73
Site 09	4,953,830	718,183	1.9	8038	311	0.58 ± 0.08	2.7	343	176
Site 11	4,955,780	718,605	3.4	9823	63	0.58 ± 0.02	2.5	360	179
Site 13	4,957,780	719,439	4.4	12,164	77	0.79 ± 0.08	2.4	281	90
Site 16	4,960,390	720,624	0.2	15,033	9	0.73 ± 0.03	2.7	304	103
Site 17	4,961,300	721,056	1.3	16,027	37	0.73 ± 0.05	2.1	334	96
Site 19	4,963,150	722,025	1.4	18,123	203	0.82 ± 0.13	2.2	290	85
Site 20	4,963,770	722,300	0.8	18,803	212	0.70 ± 0.02	2.0	280	79
Site 24	4,967,450	723,634	2.2	22,701	0	0.82 ± 0.08	2.2	324	115
Site 26	4,969,500	724,708	2.8	25,007	187	0.78 ± 0.02	2.3	316	114

Coordinate values refer to UTM zone 32 N, WGS84. All measurements lasted 30 min except site 17 (46 min) and sites 24 and 26 (50 min). Symbols as in Table 3

At some locations we observed a peak also at ~ 0.2 Hz. Such low frequency peak was observed in the same area by independent research groups as well. Nevertheless, the origin of this peak is uncertain, and we decided to cautiously limit the investigation to the 0.5–20 Hz range, which better fits the target of the present investigation. Each single-station record was split into 60 s-wide non-overlapping windows, for which amplitude spectra were computed and then smoothed using the Konno and Ohmachi window using $b = 40$ (Konno and Ohmachi 1998). The final HVSR curve is the average of the horizontal components spectra (in terms of amplitude) divided by the vertical one computed for each window. In addition, a directional analysis was performed in 10° angular increments in order to test the isotropy of the signal.

6. Results and Discussion

Given the large quantity of data acquired and their almost homogeneous quality, only the major steps of the processing, from selected locations, will be described in the following. Since upon visual inspection seismic noise signals do not convey much information, illustration will be in terms of dispersion curves for ESACs, dispersion patterns for Re-Mi surveys, and in terms of spectral ratio curves for the HVSR method.

Individual curves are interpolated to generate a 2D (frequency-location) view of the spectral ratio using the HVSR-profiling tool proposed by Herak et al. (2010), which provides the first level of analysis; subsequently, the 0.5–5 Hz portion of all HVSR curves has been inverted using the OpenHVSR code (Bignardi et al. 2016) to infer the shear wave velocity model (column “ v_s ” in Tables 3 and 4).

Examples of dispersion patterns obtained using the Re-Mi method for selected sites are shown in Fig. 4a, while the corresponding curves obtained using the ESAC method along the eastern transect B–B' are represented in Fig. 4b. All graphs clearly show a good quality down to 0.8–1.2 Hz. Given an estimated average shear wave velocity in the area ranging between 250 and 400 m/s the maximum wavelength achievable by this investigation approach

Figure 7

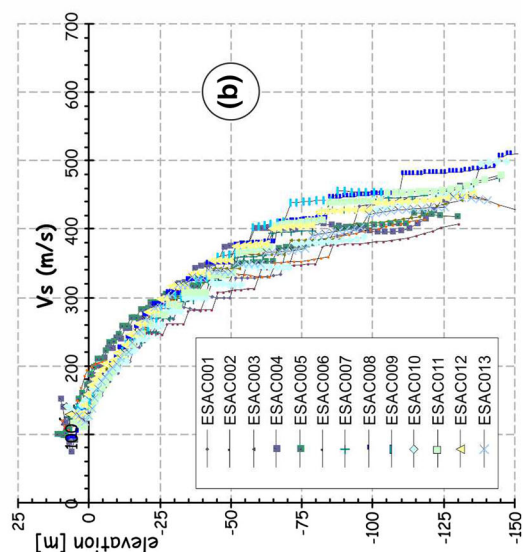
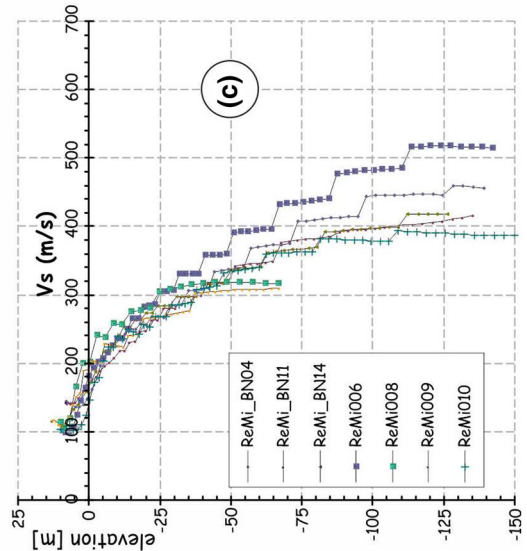
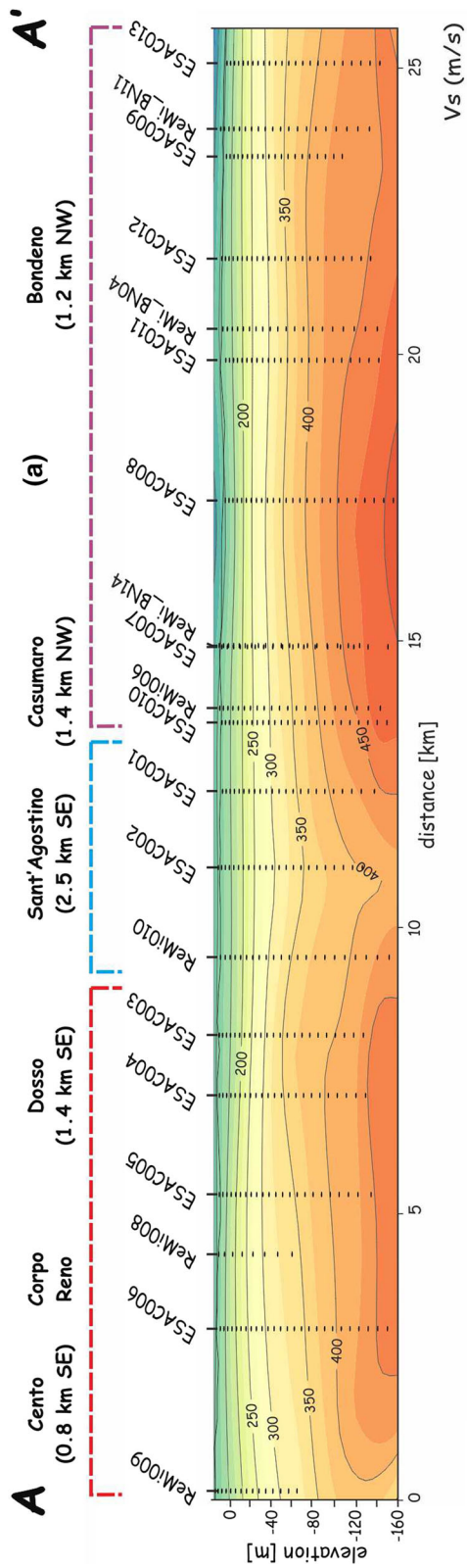
a Pseudo-2D shear-wave velocity (v_s) section along the western transect (A–A') obtained by interpolating local 1D models; colours of dashed lines on top of the profile correspond to boxes in Fig. 2c. Individual 1D velocity profiles from ESAC and Re-Mi surveys are shown in **b**, **c**, respectively

is ca. 200 m as a worst-case scenario. Considering that good resolution is achieved in ESAC up to wave lengths comparable to, or slightly longer than, the array aperture (here 130 m), we decided to limit our investigation to the first 160 m.

Figure 5 shows for reference selected examples of HVSRs pertaining to the western profile A–A', while the central section is reconstructed by applying the HVSR-profiler tool (Herak et al. 2010) to all single-station measurements. The image is obtained by spatially interpolating the amplitude of the HVSR ratio calculated for each frequency bin so that the abscissa represents the distance along the profile of the site and the ordinate axis is the frequency; the color code is associated with the amplitude of the ratio. The overall picture highlights the lateral variations of the spectral ratio along the transect and it simply provides a preliminary, though approximate, indication of the subsurface geometry. The dashed green line is used to conveniently emphasize the trend of f_0 along the transect.

In order to better exploit the HVSR measurements, we further processed these data. The whole procedure for an example site (n. 39; see Fig. 2a) is synthesized in Fig. 6. The 8-layers starting model (Fig. 6a) is derived as described in subsequent sections from the smooth ESAC result at the closest location (in this case ESAC013), and used as input for the inversion of the spectral ratio thus obtaining the local subsurface model (Fig. 6b). The experimental spectral ratio curve, error bars, and the response of the best model are shown in Fig. 6c, while Fig. 6d shows a comparison of v_s (1D) profiles from ESAC and HVSR. Finally, the theoretical dispersion curve for the final subsurface model is compared with the corresponding experimental one in Fig. 6e.

After individual processing, the local results are assembled to highlight the global picture. Shear wave



velocity models (1D) obtained by ESACs have been projected along the trace of the two profiles and their discrete information is interpolated using a minimum curvature algorithm (Briggs 1974), specifically selected in order to avoid false high/low velocity values connected to the large spatial distance between measurements as compared to the shallow depth, and to minimize surface curvature under the constraint of the surface experimental velocity values (provided by Re-Mi inversion). This procedure allowed reconstructing the interpolated pseudo-2D velocity sections along the two transects (Figs. 7, 8). As explained earlier, although some 1D models locally reached higher depths, the reconstructed sections are cautiously limited at about 160 m. Absolute elevation of the measured sites ranges between 7.1 and 14.5 m a.s.l. and between 0.2 and 4.4 m a.s.l., along the western and eastern profiles, respectively.

6.1. Western Transect A–A'

The shear wave velocity (Table 3 and Fig. 7b, c) ranges between 100 and 150 m/s, at very shallow depth, and 500 m/s, at the maximum depth in correspondence of the central-northern portion of the profile. The v_s vertical gradient is observed to be strong in the first sector (ReMi009-ESAC003) and third one (ESAC010-ESAC013) marked in red and purple in Fig. 7a, respectively. In contrast, the vertical gradient is weaker in the central sector of the profile (ReMi010-ESAC001; blue in Fig. 7a), where the maximum obtained v_s values, at 160 m b.s.l., is around 400 m/s. Such values find further justification in a recently published paper, Minarelli et al. (2016), based on downhole v_p and v_s measurements performed in a well located between Mirabello and San Carlo villages, not too far from transect A–A'. They confirmed a measured shear wave velocity of ~ 400 m/s in the 100–240 m depth range.

Inversion of HVSR curves requires a preliminary careful qualitative analysis of the microtremor characteristics, including peak clarity and stability for at least 10 or more time-windows. When the peak is clear (and is not related to the anthropogenic activity), it indicates the presence of an acoustic impedance contrast at some depth and the peak frequency represents the natural frequency (f_0) of the

Figure 8

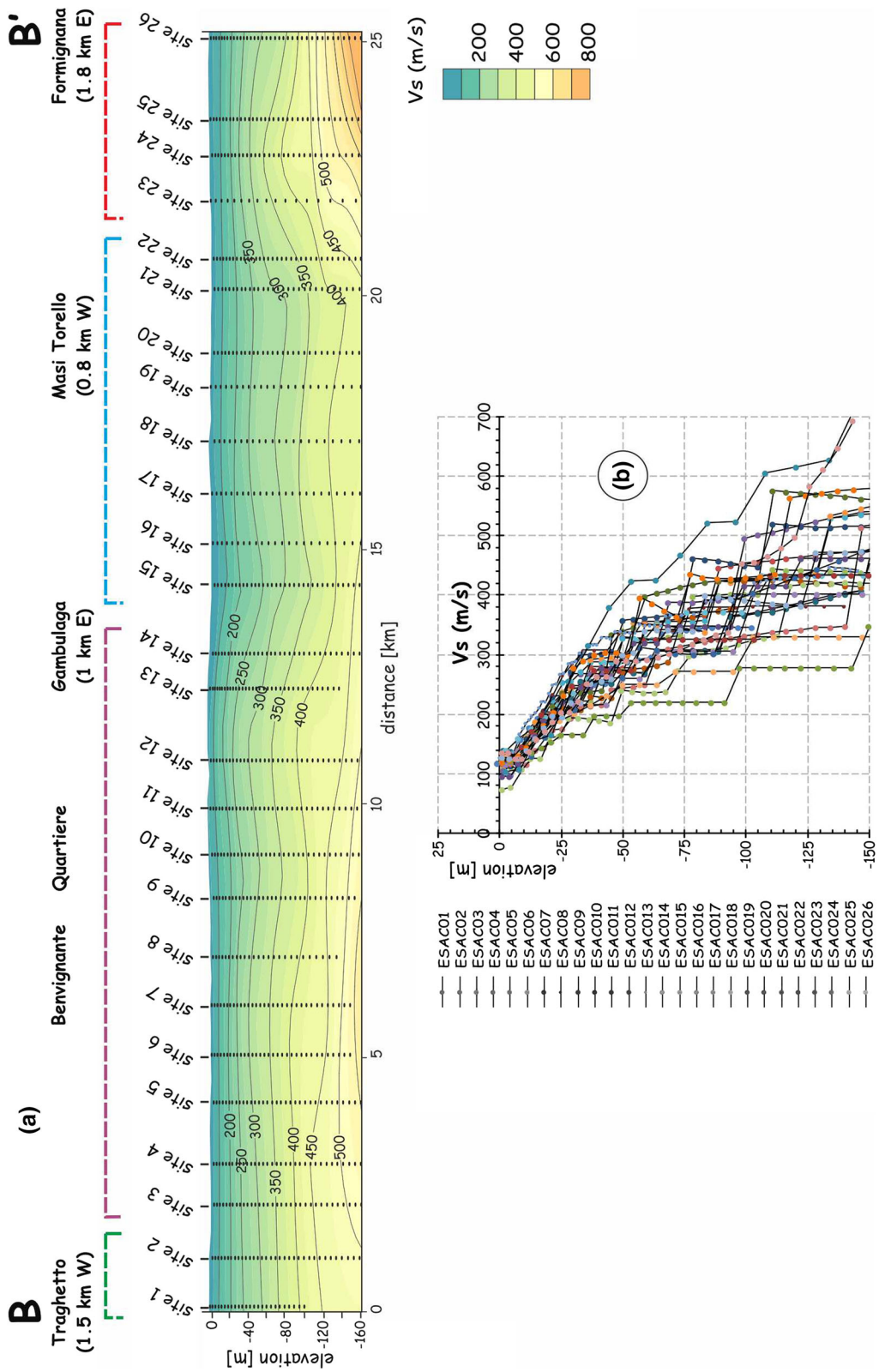
a Pseudo-2D shear-wave velocity (v_s) section along the western transect (B–B') obtained by interpolating local 1D models; colours of dashed lines on top of the profile correspond to boxes in Figs. 2d. **b** individual 1D velocity profiles from ESAC surveys

site. If the thickness is known, an approximate estimation of the shear wave velocity can be obtained. On the other hand, if the curve is flat (HVSR average value around 1), it is likely that the local velocity structure has no clear impedance contrasts (SESAME 2004).

In this context, the HVSR-profiling and the reconstructed green dashed line (Fig. 5a) highlights the occurrence of an impedance contrast whose peak is associated to frequencies ranging from a minimum of 0.52 Hz up to a maximum of 0.79 Hz (Table 3). The lowest fundamental resonance frequencies ($f_0 \leq 0.6$ Hz) are observed between sites 4 and 7, while, for the other sites f_0 is greater than 0.6 Hz. The HVSR amplitude (A_0) in the frequency section is color-coded and is systematically greater than 2.0 (Fig. 5a). The largest values ($A_0 \geq 3.5$) are observed between sites 36–39, in the northernmost portion of the profile.

Assuming that the observed lateral variation of v_s (Fig. 7a), f_0 and A_0 (Fig. 5a) do reflect lateral lithochronological variations, especially in terms of differential compaction (i.e. age) of the sediments, the two pseudo-2D sections suggest the occurrence of buried anticlinal structures associated with a 'condensed' stratigraphic sequence and, taking into account the shallow investigated depth, their recent tectonic evolution. Similar correlations have been recently proposed also for the Mirandola area (Tarabusi and Caputo 2016).

Traditionally, the main peak observed across the area was assumed to be associated to a bedrock with $v_s = 800$ m/s. Indeed, we observed that a v_s value of 800 m/s (justified by considering a cross hole survey performed by the Regione Emilia-Romagna, close to the Casaglia cemetery; Di Capua and Tarabusi 2013) was capable of reproducing our spectral ratios quite well. It should be noted however that the latter site is located in correspondence of the top of the Casaglia anticline, which is relatively distant from transect A–



A' and where the real bedrock is certainly shallower than in our investigated area and hence the velocity gradient likely stronger. Additionally, whether such a high value of v_s is actually justified for the whole area has recently been matter of discussion (Foti et al. 2009).

On the one hand, it is well known (Herak 2008) that the v_s value of the half-space can affect the amplitude of the spectral ratio, while leaving the location of the resonant peak almost unchanged. On the other hand, the principal information of HVSR resides in the peak frequency location.

Therefore, in order to investigate this aspect and to keep consistent with the lower v_s values observed by the ESAC survey, we performed few simulations and verified that even at lower v_s values, say as slow as 600 m/s (in better accordance with the ESAC results), the overall position of the frequency peaks is not altered.

The conclusion is that, while in general the passage from layers to half-space is conceptualized to correspond to the passage sediments-bedrock, in this sector of the Po Plain the real bedrock is very deep and a different velocity jump interface is in general responsible for the observed peak at f_0 .

The results provided by the inversion of the HVSR curves, compared with the available geological information, show a good agreement with some major stratigraphic unconformities (Fig. 9).

In particular, the shallower resonant interface (Fig. 9a) is likely associated to an interface separating the Middle Pleistocene sedimentary cycles (Fig. 9b) and specifically the AES7-AES6 interface (RER and ENI-AGIP 1998; Molinari et al. 2007). This stratigraphic units belong to a higher rank sedimentary cycle represented by the Upper Emiliano-Romagnolo Synthem AES (RER and ENI-AGIP 1998).

Additionally, based on the same methodological approach, we could locally infer the presence of a second deeper resonant interface (Fig. 9a) obviously corresponding to an older (Middle Pleistocene) unconformity at the base of the AEI Subsynthem (Fig. 9b; RER and ENI-AGIP 1998; Molinari et al. 2007). According to the map of the bedrock depth proposed by Martelli and Romani (2013), this sedimentary interface could be tentatively considered

as the seismic bedrock, although the v_s value associated to this stratigraphic unit (not much greater than 400 m/s) is lower than the values officially assumed for the “seismic bedrock” (EN 1998-5 2004).

The complete geological section proposed by RER and ENI-Agip (1998; Fig. 9c) clearly shows the occurrence of two buried anticline structures corresponding to the periclinal termination of the Mirandola anticline, to the south, and the Casaglia anticline, to the north. This geological setting strongly suggests that the shallow stratigraphic folding documented in this paper and constrained by the lateral shear-waves variations (for example, between 400 and 490 m/s at 140 m-depth; Fig. 7a) could be also directly associated with the tectonic activity of the blind thrusts that was persisting throughout the whole Late Quaternary.

It is also noteworthy the comparison between the obtained v_s profile (Fig. 7a) with the Structural Model of Italy (Bigi et al. 1992; Fig. 2c). Taking into account that the major faults crossed by the transects are deep and blind (e.g. Vannoli et al. 2014), while our profile investigates the shallow sediments, it is reasonably expected that their influence will reflect in weak and laterally spread deformations generating v_s gradients in correspondence of some structural ‘highs’, like the Mirandola (in its periclinal termination) and the Casaglia structure, to the south and north, respectively. In between, a tectonically “depressed” area can be inferred based on low vertical v_s gradients suggesting the presence of less compacted sediments in correspondence of the interposed syncline (blue sector in Fig. 2c).

6.2. Eastern Transect B–B'

The estimated shear wave velocities along the eastern transect (Fig. 8b) range between 100 and 150 m/s, at very shallow depth, and 500–550 m/s, at the maximum investigated depth in correspondence of the central-southern and northernmost sectors of the profile (purple and red sectors in Figs. 8a, 2d). The vertical v_s gradient is observed to be high between sites 3-to-14 and sites 23-to-26, while it is smaller in the southernmost and central sectors of the profile, at sites 1 and 2 and from sites 13-to-21, where

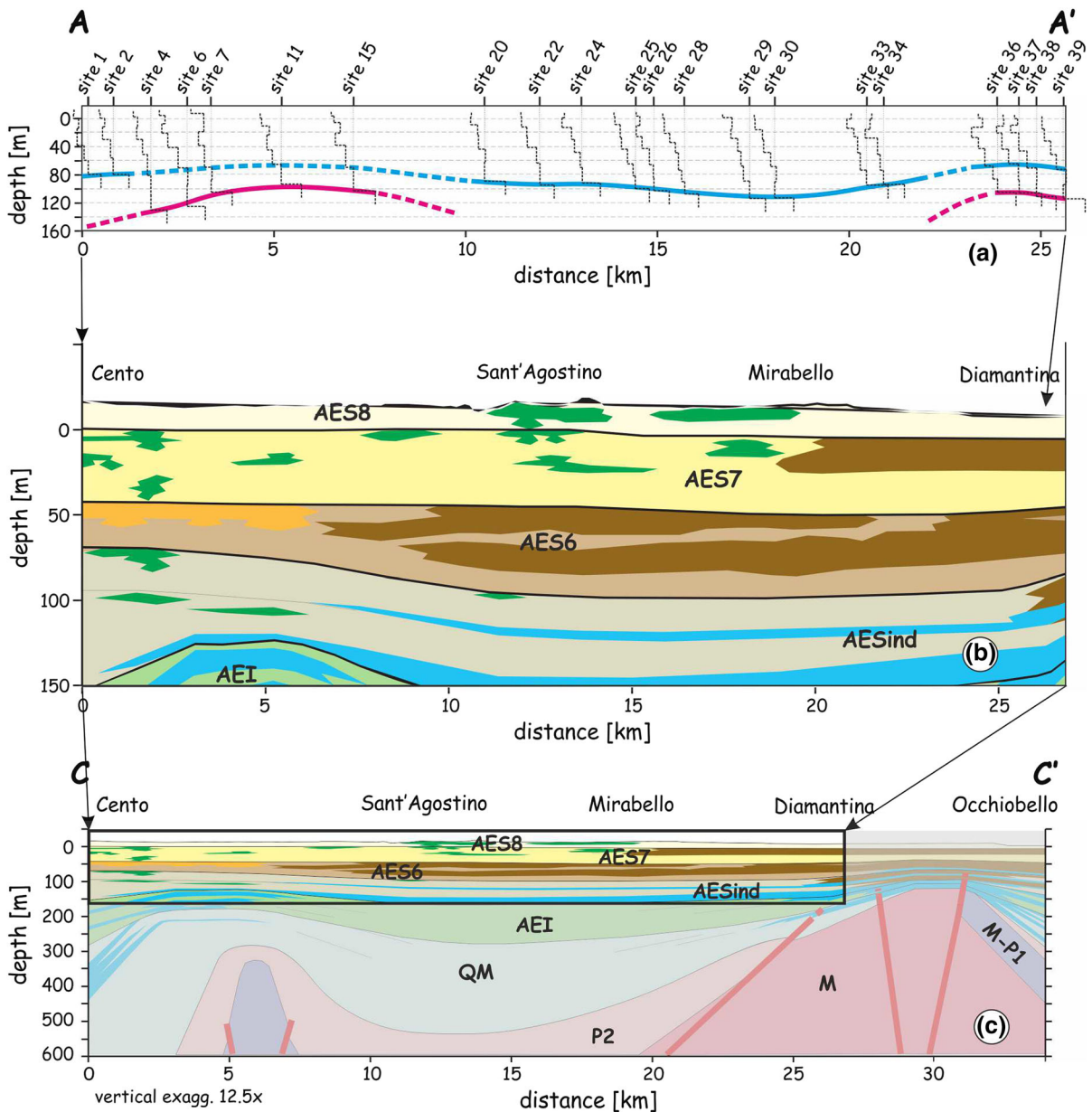


Figure 9

a Geological interpretation of the principal resonant interface associated with most significant v_s change or in correspondence of the half-space transition (blue curve), based on HVSR inversions along the western transect A–A'. The 1D v_s profiles obtained by inversion of the HVSR curves are also sketched for reference. Locally a second minor v_s change has been also observed and here interpreted as a deeper discontinuity (red curve). **b** Enlargement of the litho-stratigraphic vertical model (c) proposed by RER and ENI-Agip (1998) running almost parallel to our transect (see Fig. 2a for location). Taking into account the variable distance among the two profiles and the different approach on which the latter is based, the resonant interfaces obtained in this paper by means of noise-based geophysical methods likely correspond to interfaces close to the AES7–AES6 boundary and the base of AESind Subsynthem, respectively. *AEI* Lower Emiliano-Romagnolo Subsynthem (Middle Pleistocene), *AESind* undifferentiated Emiliano-Romagnolo Subsynthem (Middle Pleistocene), *AES6* Bozzano Subsynthem (Middle Pleistocene), *AES7* Villa Verrucchio Subsynthem (Late Pleistocene), *AES8* Ravenna Subsynthem (Late-Pleistocene–Present)

maximum obtained v_s values at 160 m b.s.l. is around 400–450 m/s (green and blue sectors in Figs. 8a, 2d). Similar to the western transect, several regularly spaced HVSR stations were acquired using both the same equipment and acquisition parameters and all HVSR curves were inverted using v_p and v_s values provided by the ESAC investigation following the same procedure described in the previous sections (Fig. 6). The reconstructed frequency-distance section (not shown here), reveals the presence of an impedance contrast whose peaks are associated with frequencies ranging from a minimum of 0.58 Hz up to a maximum of 0.85 Hz (Table 4). Low fundamental resonance frequencies ($f_0 < 0.7$ Hz) are observed at sites 06, 09 and 11, while, for sites 02, 03, 04, and 05 (to the south), 19 and 24 (to the north) f_0 is greater than 0.8 Hz. The HVSR amplitude (A_0) within the transect varies between 2.0 and 3.1 (Table 4).

The results provided by HVSR inversions also along the eastern transect were then compared with the available geological information consisting of three geological profiles crossing the investigated transect at high angle (Fig. 2b). They show good agreement with some major stratigraphic unconformities (Fig. 10). Similar to the western A–A' transect, the shallower principal resonant interface that has been detected in B–B' could correspond to the AES7–AES6 interface (Middle Pleistocene sedimentary cycles; RER and ENI-AGIP 1998; Molinari et al. 2007), while the locally visible deeper interface seems to correspond to the top of the AEI Subsynthem (Fig. 10b).

Also in this case, the comparison with the Structural Model of Italy (Bigi et al. 1992, Fig. 2d) shows a good fit between the reconstructed 'shallow' lateral variations of v_s and the deeper buried tectonic structures. In particular, velocity gradients are higher in correspondence of some major thrust faults and associated anticlines, namely the Argenta Thrust to the south and the Eastern Ferrara structures to the north (purple and red sectors in Fig. 2d). In between and in the southernmost sector of the profile, two tectonically 'depressed' areas can be inferred based on low vertical v_s gradients suggesting the presence of softer sediments.

7. Concluding Remarks

The present study provides some insight on the dynamic properties of a portion of the eastern sector of the Po Plain and particularly of the central portion of the Ferrara Arc, responsible of the historical earthquakes that hit Ferrara in 1570 and Argenta in 1624 ($I_0 = \text{VII–VIII}$; Rovida et al. 2016; Guidoboni et al. 2018).

Due to the combination of a regionally fast subsidence and correspondingly high sedimentary rates as well as of a relatively low tectonic activity, the thrusts developed within the Po Plain are all blind (Figs. 2c, d). However, the highly variable thickness of the Quaternary sequences from several hundreds to few tens of meters in correspondence of the growing Mirandola, Casaglia, Ferrara, and Argenta anticlines, clearly reflects the concurrent role and the recent activity of the blind thrusts belonging to the major Ferrara Arc.

In order to investigate the shallow subsurface, we purposely selected two 27 km-long transects oriented almost perpendicularly to the regional trend of the buried structures, investigating them on the basis of diverse passive seismic methods (i.e. ESAC, Re-Mi and HVSR). Based on numerous 1D subsurface models obtained at regularly spaced locations along the transects it was possible to reconstruct the corresponding 2D shear wave velocity profile. By means of low-cost geophysical surveys (cost-effective equipment and very small teams), our approach, firstly, highlighted the recent tectonic activity of the buried structures underlying this sector of the Po Plain. In particular, assuming that the v_s and the fundamental resonance frequency patterns are determined by both vertical and lateral lithological variations, the reconstructed pseudo-2D sections document the occurrence of reduced (i.e. condensed) stratigraphic successions in correspondence of the major anticline structures. This is also confirmed by the 'constrained' inversion of the HVSR curves used to infer the depth(s) of significant reflectors corresponding to the observed frequency(ies) peaks that resulted to be linked to some major stratigraphic unconformities.

Secondly, and beyond the geological and tectonic information obtained along the two transects, all the

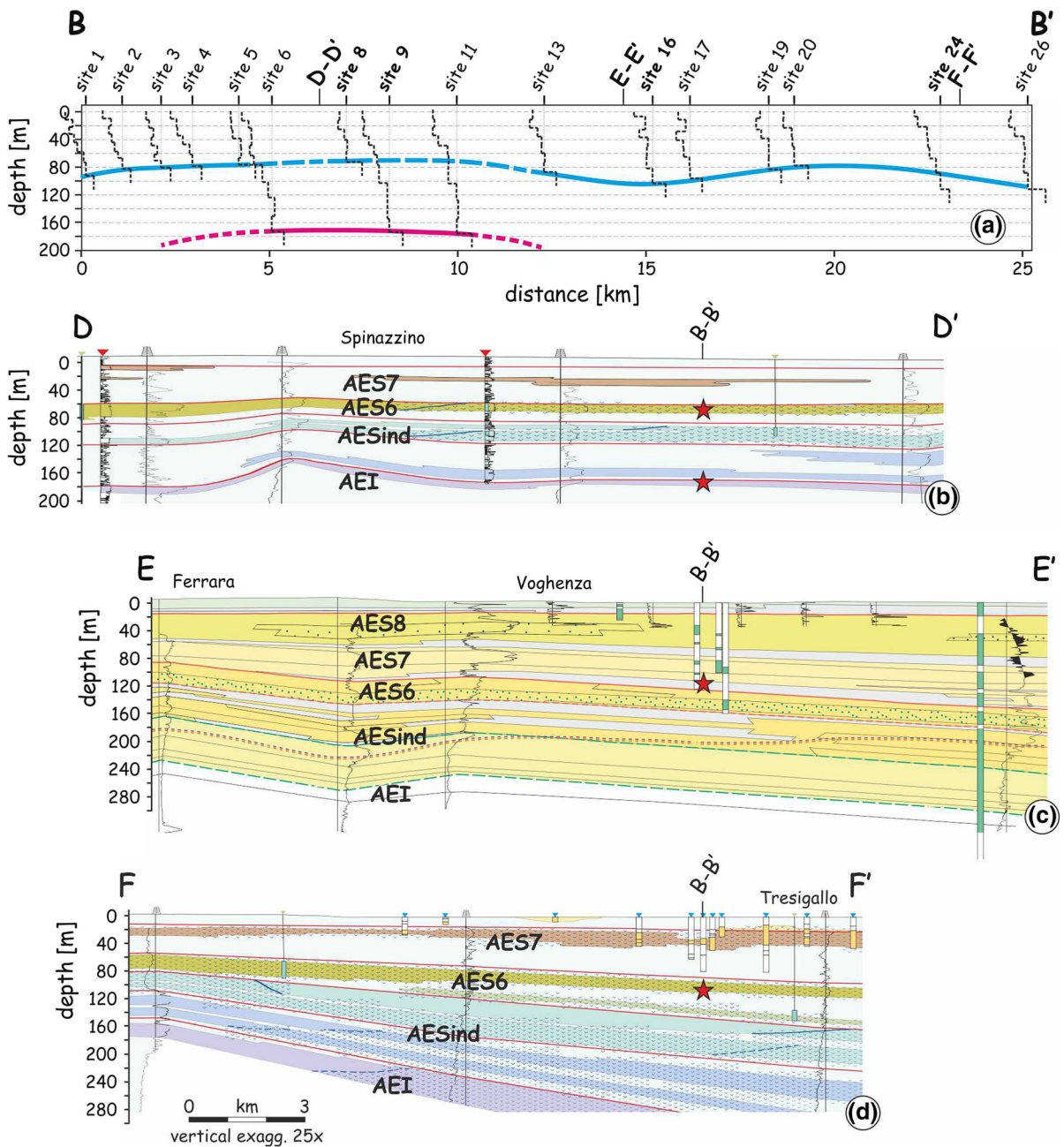


Figure 10

a Geological interpretation of the principal resonant interface associated with most significant v_s change or in correspondence of the half-space transition (blue curve), based on HVSR inversions along the western transect B-B'. The 1D v_s profiles obtained by inversion of the HVSR curves are also sketched for reference. Locally a second minor v_s change has been also observed and here interpreted as a deeper discontinuity (red curve). In panels **b-d** are represented litho-stratigraphic vertical models (modified from Molinari et al. 2007; ISPRA 2009) crossing roughly perpendicular to our transect (see Fig. 2b for location). Stars indicate the position of the resonant interfaces obtained in this paper corresponding to interfaces close to the AES7-AES6 boundary and the top of the AEI Subsystem, respectively. Labels are as in Fig. 9

measured sites within this sector of the Po Plain show an almost homogeneous distribution of v_s in the shallowest 30 m. As above mentioned, this information is crucial in seismic microzoning studies because it is typically exploited to characterize the v_{s30} parameter (commonly used to evaluate the local amplification, i.e. the local expected PGA). This research clearly documents how at slightly greater depths, say between 30 and 150 m, the subsurface is, in contrast, strongly differentiated with undoubtedly different seismic responses at different sites. Accordingly, we suggest that the v_{s30} approach commonly used in microzoning studies is too simplistic because it ignores the presence of deeper discontinuities and may lead to underestimating the local seismic hazard. Therefore, the described methodology and the achieved results may reveal valuable in the estimation of the local site response, which is known to strongly depend on the careful evaluation of the shear wave velocity profile down to the seismic bedrock.

Acknowledgements

The study has benefited from funding provided by the Italian Presidenza del Consiglio dei Ministri—Dipartimento di Protezione Civile (DPC). The findings and conclusions in this article are those of the author(s) and do not necessarily represent DPC official opinion and policies. Additionally, part of the data collection benefited from funding by the Ferrara Province administration and the city of Bondeno administration. We thank the Editor and two anonymous reviewers that contributed to improve a former version of the manuscript.

Publisher's Note Springer Nature remains neutral with regard to jurisdictional claims in published maps and institutional affiliations.

REFERENCES

- Abu Zeid, N. (2016). Geophysical characterization of liquefied terrains using the electrical resistivity and induced polarization methods: The case of the Emilia earthquake 2012. In S. D'Amico (Ed.), *Earthquakes and their impact on society* (pp. 213–232). Berlin: Springer. https://doi.org/10.1007/978-3-319-21753-6_8.
- Abu Zeid, N., Bignardi, S., Caputo, R., Santarato, G., & Stefani, M. (2012). Electrical resistivity tomography investigation on coseismic liquefaction and fracturing at San Carlo, Ferrara Province, Italy. *Annals of Geophysics*, 55, 713–716. <https://doi.org/10.4401/ag-6149>.
- Abu Zeid, N., Corradini, E., Bignardi, S., Nizzo, V., & Santarato, G. (2017). The passive seismic technique 'HVSr' as a reconnaissance tool for mapping paleo-soils: The case of the Pilastrì archaeological site, northern Italy. *Archaeological Prospection*. <https://doi.org/10.1002/arp.1568>.
- Abu Zeid, N., Corradini, E., Bignardi, S., & Santarato, G. (2016). Unusual geophysical techniques in archaeology—HVSr and induced polarization, a case history. *22nd Europe Meeting Environment Engineering Geophysics, NSAG-2016*. <https://doi.org/10.3997/2214-4609.201602027>.
- Abu-Zeid, N., Bignardi, S., Caputo, R., Mantovani, A., Tarabusi, G., & Santarato, G. (2013). *Acquisition of V_s profiles across the Casaglia anticline (Ferrara Arc)*. DPC-INGV-S1 Project, Final Report, pp. 42–46.
- Abu-Zeid, N., Bignardi, S., Caputo, R., Mantovani, A., Tarabusi, G., & Santarato, G. (2014). Shear-wave velocity profiles across the Ferrara Arc: A contribution for assessing the recent activity of blind tectonic structures. *33th Conference GNGTS, Proceedings*, 1, 117–122.
- AGIP-MINERARIA. (1959). Campi gassiferi padani. *Atti Convegno 'Giacimenti Gassiferi dell'Europa Occidentale'*. Rome: Accademia Nazionale dei Lincei.
- Aki, K. (1957). Space and time spectra of stationary stochastic waves, with special reference to microtremors. *Bulletin Earth Research Institute*, 35, 415–456.
- Aki, K. (1964). A note on the use of microseisms in determining the shallow structures of the earth's crust. *Geophysics*, 29, 665–666.
- Albarello, D., & Castellaro, S. (2011). Tecniche sismiche passive: Indagini a stazione singola. *Ingegneria Sismica*, XXVIII(2), 32–62.
- Albarello, D., Cesi, C., Eulili, V., Guerrini, F., Lunedei, E., Paolucci, E., et al. (2011). The contribution of the ambient vibration prospecting in seismic microzoning: An example from the area damaged by the 26th April 2009 L'Aquila (Italy) earthquake. *Bulletin Geof Teor Application*, 52(3), 513–538.
- Amorosi, A. (2008). Delineating aquifer geometry within sequence stratigraphic framework: Evidence from Quaternary of the Po River Basin Northern Italy. *GeoActa, Special Publication*, 1, 1–14.
- Amorosi, A., & Colalongo, M. (2005). The linkage between alluvial and coeval nearshore marine succession: Evidence from the Late Quaternary record of the Po River Plain, Italy. In M. Blum & S. Marriott (Eds.), *Fluvial Sedimentology*. Oxford: IAS Special Publication.
- AQUATER. (1976). *Elaborazione dei dati geofisici relativi alla Dorsale Ferrarese*. Rapporto inedito per ENEL.
- AQUATER. (1978). *Interpretazione dei dati geofisici delle strutture plioceniche e Quaternarie della Pianura Padana e Veneta*. Rapporto inedito per ENEL.
- AQUATER. (1980). *Studio del nannoplancton calcareo per la datazione della scomparsa della Hyaline baltica nella Pianura Padana e Veneta*. Rapporto inedito per ENEL.

- AQUATER-ENEL. (1981). *Elementi di neotettonica del territorio italiano*. Volume speciale, Roma.
- Argnani, A., Barbacini, G., Bernini, M., Camurri, F., Ghielmi, M., Papani, G., et al. (2003). Gravity tectonics driven by Quaternary uplift in the Northern Apennines: Insights from the La Spezia-Reggio Emilia Geo-Transsect. *Quaternary International*, 101(102), 13–26.
- Argnani, A., & Frugoni, F. (1997). Foreland deformation in the Central Adriatic and its bearing on the evolution of the Northern Apennines. *Annales Geophysicae*, 40(3), 77–780.
- Asten, M. W. (1978). Geological control of the three-component spectra of Rayleigh-wave microseisms. *Bulletin of the Seismological Society of America*, 68(6), 1623–1636.
- Asten, M. W., & Henstridge, J. D. (1984). Arrays estimators and the use of microseisms for reconnaissance of sedimentary basins. *Geophysics*, 49(11), 1828–1837.
- Bard, P.-Y. (1999). Microtremor measurements: A tool for site estimation? State-of-the-art paper. In Okada & Sasatani (Eds) *2nd International Symposium Effects of Surface Geology on seismic motion, Yokohama, December 1–3, 1998, Irikura, Kudo, Balkema 1999* (vol. 3, pp. 1251–1279).
- Bertotti, G., Capozzi, R., & Picotti, V. (1998). Extension controls Quaternary tectonics, geomorphology and sedimentation of the N-Apennines foothills and adjacent Po Plain (Italy). *Tectonophysics*, 282, 291–301.
- Bigi G., Bonardini G., Catalano R., Cosentino D., Lentini F., Parlotto M. Sartori R., Scandone P. & Turco E. (1992): Structural model of Italy, 1:500,000. Consiglio Nazionale delle Ricerche, Rome.
- Bignardi, S. (2017). The uncertainty of estimating the thickness of soft sediments with the HVSR method: A computational point of view on weak lateral variations. *Journal of Applied Geophysics*, 145C, 28–38. <https://doi.org/10.1016/j.jappgeo.2017.07.017>.
- Bignardi, S., Fedele, F., Santarato, G., Yezzi, A., & Rix, G. (2013). Surface waves in laterally heterogeneous media. *Journal of Engineering Mechanics*, 139(9), 1158–1165. [https://doi.org/10.1061/\(ASCE\)CR.1943-7889.0000566](https://doi.org/10.1061/(ASCE)CR.1943-7889.0000566).
- Bignardi, S., Fiussello, S., & Yezzi, A.J. (2018b), Free and improved computer codes for hvsr processing and inversions. In *31st SAGEEP, Nashville, TN, USA March 25–29, 2018, Proceedings*.
- Bignardi, S., Mantovani, A., & Abu, Zeid N. (2016). OpenHVSR: Imaging the subsurface 2D/3D elastic properties through multiple HVSR modeling and inversion. *Computers and Geosciences*, 93, 103–113. <https://doi.org/10.1016/j.cageo.2016.05.009>.
- Bignardi, S., Santarato, G., & Abu Zeid, N. (2014). Thickness variations in layered subsurface models—Effects on simulated MASW. In *76th EAGE conference & exhibition, Ext. abstract, WS6P04*. <https://doi.org/10.3997/2214-4609.20140540>.
- Bignardi, S., Yezzi, A. J., Fiussello, S., & Comelli, A. (2018a). OpenHVSR—Processing toolkit: Enhanced HVSR processing of distributed microtremor measurements and spatial variation of their informative content. *Computers and Geosciences*, 120, 10–20. <https://doi.org/10.1016/j.cageo.2018.07.006>.
- Boatwright, J., Fletcher, J., & Fumal, T. (1991). A general inversion scheme for source, site and propagation characteristics using multiply recorded sets of moderate-sized earthquakes. *Bulletin of the Seismological Society of America*, 81, 1754–1782.
- Boccaletti, M., Bonini, M., Corti, G., Gasperini, P., Martelli, L., Piccardi, L., Tanini, C., & Vannucci G. (2004). *Seismotectonic Map of the Emilia-Romagna Region, 1:250000*. Regione Emilia-Romagna—CNR.
- Boccaletti, M., Corti, G., & Martelli, L. (2011). Recent and active tectonics of the external zone of the Northern Apennines (Italy). *International Journal of Earth Sciences*, 100, 1331–1348.
- Bonnefoy-Claudet, S., Cornou, C., Bard, P., Cotton, F., Moczo, P., Kristek, J., et al. (2006). H/V ratio: A tool for site effects evaluation. Results from 1-D noise simulations. *Geophysical Journal International*, 167, 827–837.
- Borcherdt, R.D. (2012). VS30—A site-characterization parameter for use in building codes, simplified earthquake resistant design, GMPEs, and ShakeMaps. In *15th WCEE, Lisbon, 24–28 September 2012*.
- Borcherdt, R. D., & Glassmoyer, G. (1992). On the characteristics of local geology and their influence on ground motions generated by the Loma Prieta earthquake in the San Francisco Bay region, California. *Bulletin of the Seismological Society of America*, 82, 603–641.
- Bordoni, P., Azzara, R., Cara, F., Cogliano, R., Cultrera, G., Di Giulio, G., et al. (2012). Preliminary results from EMERSITO, a rapid response network for site-effect studies. *Annales Geophysicae*, 55(4), 599–607.
- Briggs, I. C. (1974). Machine contouring using minimum curvature. *Geophysics*, 39, 39–48.
- Burrato, P., Ciucci, F., & Valensise, G. (2003). An inventory of river anomalies in the Po Plain, northern Italy: Evidence for active blind thrust faulting. *Annales Geophysicae*, 46(5), 865–882.
- Burrato, P., Vannoli, P., Fracassi, U., Basili, R., & Valensise, G. (2012). Is blind faulting truly invisible? Tectonic-controlled drainage evolution in the epicentral area of the May 2012, Emilia-Romagna earthquake sequence (northern Italy). *Annales Geophysicae*, 55(4), 525–531. <https://doi.org/10.4401/ag-6182>.
- Capon, J. (1969). High-resolution frequency-wavenumber spectrum analysis. *IEEE*, 57, 1408–1419.
- Caputo, R., & Papathanasiou, G. (2012). Ground failure and liquefaction phenomena triggered by the 20 May, 2012 Emilia-Romagna (Northern Italy) earthquake: Case study of Sant’Agostino-San Carlo-Mirabello zone. *National Hazards Earth System Sciences*, 12(11), 3177–3180. <https://doi.org/10.5194/nhess-12-3177-2012>.
- Caserta, A., Zahradnik, J., & Plicka, V. (1999). Ground motion modeling with a stochastically perturbed excitation. *Journal of Seismology*, 3, 45–59.
- Castellari, A., Eva, C., Giglia, G., Vai, G., Rabbi, E., Pini, G., et al. (1985). Analisi strutturale del Fronte Appenninico Padano. *Giornale di Geologia*, 47, 47–75.
- Costa, M. (2003). The buried, apenninic arcs of the Po Plain and Northern Adriatic Sea (Italy): A new model. *Bollettino della Società Geologica Italiana*, 122, 3–23.
- D’Alessandro, A., Luzio, D., Martorana, R., & Capizzi, P. (2016). Selection of time windows in the horizontal-to-vertical noise spectral ratio by means of cluster analysis. *Bulletin of the Seismological Society of America*, 106(2), 560–574. <https://doi.org/10.1785/0120150017>.
- Di Capua, G., & Tarabusi, G. (2013). *Site specific hazard assessment in priority areas*. DPC-INGV-S2 Project, Annex 3 to Deliverable 4.1.
- EN 1998-5. (2004). Eurocode 8: Design of structures for earthquake resistance—Part 5: Foundations, retaining structures and geotechnical aspects. In *CEN European Committee for Standardization, Bruxelles, Belgium*.

- Foti, S., Comina, C., Boiero, D., & Socco, L. V. (2009). Non-uniqueness in surface wave inversion and consequences on seismic site response analyses. *Soil Dynamics and Earthquake Engineering*, 29(6), 982–993.
- Gallipoli, M. R., Mucciarelli, M., Eeri, M., Gallicchio, S., Tropeano, M., & Lizza, C. (2004). Horizontal to Vertical Spectral Ratio (HVSr) measurements in the area damaged by the 2002 Molise, Italy earthquake. *Earthquake Spectra*, 20(1), 81–93. <https://doi.org/10.1193/1.1766306>.
- Garofalo, F., Foti, S., Hollender, F., Bard, P. Y., Cornou, C., Cox, B. R., et al. (2016a). InterPACIFIC project: Comparison of invasive and non-invasive methods for seismic site characterization. Part II: Inter-comparison between surface wave and borehole methods. *Soil Dynamic Earthquake Engineering*, 82, 241–254. <https://doi.org/10.1016/j.soildyn.2015.12.009>.
- Garofalo, F., Foti, S., Hollender, F., Bard, P. Y., Cornou, C., Cox, B. R., et al. (2016b). InterPACIFIC project: Comparison of invasive and non-invasive methods for seismic site characterization. Part I: Intra-comparison of surface wave methods. *Soil Dynamic Earthquake Engineering*, 82, 222–240. <https://doi.org/10.1016/j.soildyn.2015.12.010>.
- Guidoboni E., Ferrari G., Mariotti D., Comastri A., Tarabusi G., Sgattoni G., & Valensise G. (2018). *CFT5Med, Catalogo dei Forti Terremoti in Italia (461 a.C.-1997) e nell'area Mediterranea (760 a.C.-1500)*. Istituto Nazionale di Geofisica e Vulcanologia (INGV). <http://storing.ingv.it/cfti/cfti5/>. Accessed 4 Feb 2019.
- Gutenberg, B. (1958). Microseisms. *Advances in Geophysics*, 5, 53–92.
- Herak, M. (2008). ModelHVSr—a Matlab tool to model horizontal-to-vertical spectral ratio of ambient noise. *Computers Geoscience*, 35, 1514–1526.
- Herak, M., Allegretti, I., Herak, D., Kuk, K., Kuk, V., Maric, K., et al. (2010). HVSr of ambient noise in Ston (Croatia): Comparison with theoretical spectra and with the damage distribution after the 1996 Ston-Slano earthquake. *Bulletin of Earthquake Engineering*, 8, 483–499.
- ISPRA. (2009). *Carta Geologica d'Italia alla scala 1:50.000, Foglio 203 Poggio Renatico*. Coord. Scient.: U. Cibin, Regione Emilia-Romagna. ISPRA, Servizio Geologico d'Italia, Regione Emilia-Romagna, SGSS.
- Kanai, K., Osada, T., & Tanaka, T. (1954). Measurement of the microtremors. *Bulletin Earthquake Research Institute, University of Tokyo*, 32, 199–209.
- Konno, K., & Ohmachi, T. (1998). Ground-motion characteristics estimated from spectral ratio between horizontal and vertical components of microtremor. *Bulletin of the Seismological Society of America*, 88(1), 228–241.
- Lai, C. G., Foti, S., Godio, A., Rix, G. J., Sambuelli, L., & Socco, L. V. (2000). Caratterizzazione geotecnica dei terreni mediante l'uso di tecniche geofisiche. *Rivista Italiana di Geotecnica*, 34(3), 99–118.
- Laurenzano, G., Priolo, E., Barnaba, C., Gallipoli, M.R., Klin, P., Mucciarelli, M., & Romanelli, M. (2013). *Studio sismologico per la caratterizzazione della risposta sismica di sito ai fini della microzonazione sismica di alcuni comuni della regione Emilia-Romagna—Relazione sulla attività svolta*. Rel. OGS 2013/74 Sez. CRS 26, 31 luglio.
- Louie, J. N. (2001). Faster, better: Shear-wave velocity to 100 meters depth from refraction microtremor arrays. *Bulletin of the Seismological Society of America*, 91(2), 347–364.
- Lucchi, F. R. (1986). Oligocene to Recent foreland basins of northern Apennines. In P. A. Allen & P. Homewood (Eds.), *Foreland basins* (Vol. 8, pp. 105–139). Oxford: IAS.
- Lunedei, E., & Albarello, D. (2010). Theoretical HVSr curves from full wavefield modelling of ambient vibrations in a weakly dissipative layered Earth. *Geophysical Journal International*, 181, 1093–1108. <https://doi.org/10.1111/j.1365-246X.2010.04560.x>.
- Lunedei, E., & Albarello, D. (2015). Horizontal-to-vertical spectral ratios from a full-wavefield model of ambient vibrations generated by a distribution of spatially correlated surface sources. *Geophysical Journal International*, 201(2), 1140–1153. <https://doi.org/10.1093/gji/ggv046>.
- Mantovani, A., Valkaniotis, S., Rapti, D., & Caputo, R. (2018). Mapping the palaeo-Piniada Valley, Central Greece, based on systematic microtremor analyses. *Pure and Applied Geophysics*, 175, 865–881. <https://doi.org/10.1007/s00024-017-1731-7>.
- Margheriti, L., Azzara, R., Cocco, M., Delladio, A., & Nardi, A. (2000). Analyses of borehole broadband recordings: Test site in the Po basin, Northern Italy. *Bulletin of the Seismological Society of America*, 90, 1454–1463.
- Martelli, L., & Romani, M. (2013). *Microzonazione Sismica e analisi della Condizione Limite per l'Emergenza delle aree epicentrali dei terremoti della pianura emiliana di maggio-giugno 2012*. (Ordinanza del Commissario Delegato—Presidente della Regione Emilia-Romagna n. 70/2012). Relazione illustrativa. <http://ambiente.regione.emilia-romagna.it/geologia/temi/sismica/speciale-terremoto/sisma-2012-ordinanza-70-13-11-2012-cartografia>. Accessed 4 Feb 2019.
- Martorana, R., Capizzi, P., D'Alessandro, A., Luzio, D., Di Stefano, P., Renda, P., et al. (2018). Contribution of HVST measures for seismic microzonation studies. *Annals of Geophysics*, 61(2), 225.
- Masetti, D., Fantoni, R., Romano, R., Sartorio, D., & Trevisani, E. (2012). Tectonostratigraphic evolution of the Jurassic extensional basins of the eastern southern Alps and Adriatic foreland based on an integrated study of surface and subsurface data. *American Association Petroleum Geol. Bulletin*, 96(11), 2065–2089. <https://doi.org/10.1306/03091211087>.
- Massolino, G., Abu Zeid, N., Bignardi, S., Gallipoli, M.R., Stabile, T.A., Rebez, A., & Mucciarelli, M. (2018). Ambient vibration tests on a building before and after the 2012 Emilia (Italy) earthquake, and after seismic retrofitting. *16th ECEE, June 2018, Thessaloniki, Greece*.
- Matsushima, S., Hirokawa, T., De Martin, F., Kawase, H., & Sánchez-Sesma, F. J. (2014). The effect of lateral heterogeneity on horizontal-to-vertical spectral ratio of microtremors inferred from observation and synthetics. *Bulletin of the Seismological Society of America*, 104(1), 381–393. <https://doi.org/10.1785/0120120321>.
- McMechan, G. A., & Yedlin, M. J. (1981). Analysis of dispersive waves by wave field transformation. *Geophysics*, 46, 869–874.
- Minarelli, L., Amoroso, S., Tarabusi, G., Stefani, M., & Pulelli, G. (2016). Down-hole geophysical characterization of middle-upper Quaternary sequences in the Apennine Foredeep, Mirabello, Italy. *Annals of Geophysics*, 59(5), 543. <https://doi.org/10.4401/ag-7114>.
- Molinari, F., Boldrini, G., Severi, P., Duroni, G., Rapti-Caputo, D., & Martinelli, G. (2007). *Risorse idriche sotterranee della Provincia di Ferrara*. Regione Emilia-Romagna (DB MAP eds.). Florence, p. 61.

- Mucciarelli, M., Di, Gallipoli M. R., Giacomo, D., Di Nota, F., & Nino, E. (2005). The influence of wind on measurements of seismic noise. *Geophys. J. Int.*, *161*(2), 303–308. <https://doi.org/10.1111/j.1365-246X.2004.02561.x>.
- Mulargia, F., & Castellaro, S. (2016). HVSR deep mapping tested down to ~ 1.8 km in Po Plane Valley, Italy. *Physics Earth Planetenary International*, *261*, 17–23. <https://doi.org/10.1016/j.pepi.2016.08.002>.
- Nakamura, Y. (1989). A method for dynamic characteristics estimation of subsurface using microtremor on the ground surface. *Quarterly Reports RTRI*, *30*, 25–33.
- Nardon, S., Marzorati, D., Bernasconi, A., Cornini, S., Gonfalini, M., Romano, A., et al. (1991). Fractured carbonate reservoir characterisation and modelling: A multidisciplinary case study from the Cavone oil field, Italy. *First Break*, *9*(12), 553–565.
- Nogoshi, M., & Igarashi, T. (1970). On the propagation characteristics of microtremors. *Journal of Seismological Society Japan*, *23*, 264–280.
- Obradovic, M., Abu, Zeid N., Bignardi, S., Bolognesi, M., Peresani, M., Russo, P., et al. (2015). *High resolution geophysical and topographical surveys for the characterization of Fumane Cave Prehistoric Site*. Italy: Near Surface Geoscience. <https://doi.org/10.3997/2214-4609.201413676>.
- Ohori, M., Nobata, A., & Wakamatsu, K. (2002). A comparison of ESAC and FK methods of estimating phase velocity using arbitrarily shaped microtremor arrays. *Bulletin of the Seismological Society of America*, *92*(6), 2323–2332.
- Okada, H. (1986). *A research on long period microtremor array observations and their time and spatial characteristics as probabilistic process*. Report of a Grant-in-Aid for Co-operative Research (A) No. 59340026 supported by the Scientific Research Fund in 1985.
- Okada, H. (2003). *The Microtremor survey method*. Geophysics. Monograph Series, SEG, p. 129.
- Paolucci, E., Albarello, D., D'Amico, S., Lunidei, E., Martelli, L., Mucciarelli, M., et al. (2015). A large scale ambient vibration survey in the area damaged by May–June 2012 seismic sequence in Emilia Romagna, Italy. *Bulletin Earthquake Engineering*, *13*(11), 3187–3206.
- Patacca, E., & Scandone, P. (1989). Post-Tortonian mountain building in the Apennines. The role of the passive sinking of a relic lithospheric slab. In: Boriani AM. et al. (Eds) *The Lithosphere in Italy*. Atti dei Convegni Lincei (vol. 80, pp. 157–176).
- Papathanassiou, G., Mantovani, A., Tarabusi, G., Rapti, D., & Caputo, R. (2015). Assessment of liquefaction potential for two liquefaction prone area considering the May 20, 2012 Emilia (Italy) earthquake. *Engineering Geology*, *189*, 1–16. <https://doi.org/10.1016/j.enggeo.2015.02.002>.
- Park, C., Miller, R., & Xia, J. (1999). Multichannel analysis of surface waves. *Geophysics*, *64*, 800–808.
- Picotti, V., & Pazzaglia, F. (2008). A new active tectonic model for the construction of the Northern Apennines mountain front near Bologna (Italy). *Journal of Geophysics Research*, *113*, B08412. <https://doi.org/10.1029/2007JB005307>
- Pieri, M., & Groppi, G. (1981). *Subsurface geological structure of the Po Plain, Italy*. Consiglio Nazionale delle Ricerche, Progetto finalizzato Geodinamica, sottoprogetto Modello Strutturale, pubbl. N° 414, Roma, p. 13.
- Pondrelli, S., Salimbeni, S., Perfetti, P., & Danecek, P. (2012). Quick regional centroid moment tensor solutions for the Emilia 2012 (northern Italy) seismic sequence. *Annales Geophysicae*, *55*(4), 615–621. <https://doi.org/10.4401/ag-6146>.
- Priolo, E., Romanelli, M., Barnaba, C., Mucciarelli, M., Laurenzano, G., Dall'olio, L., et al. (2012). The ferrara thrust earthquakes of May–June 2012—Preliminary site response analysis at the sites of the OGS temporary network. *Annals of Geophysics*, *55*(4), 591–597. <https://doi.org/10.4401/ag-6172>.
- RER and ENI-Agip. (1998). *Riserve idriche sotterranee della Regione Emilia-Romagna*. In G. M. Di Dio (Ed.), *Regione Emilia-Romagna, ufficio geologico—ENI-Agip, Divisione Esplorazione & Produzione* (p. 120). Firenze: S.EL.CA.
- Rovida, A., Locati, M., Camassi, R., Lolli, B., & Gasperini, P. (Eds.). (2016). *CPTI15, the 2015 version of the parametric catalogue of Italian earthquakes*. Rome: Istituto Nazionale di Geofisica e Vulcanologia. <https://doi.org/10.6092/ingv.it-cpti15>.
- Scherbaum, F., Hinzen, K. G., & Ohrnberger, M. (2003). Determination of shallow shear wave velocity profiles in the Cologne/Germany area using ambient vibrations. *Geophysical Journal International*, *152*, 597–612.
- Scrocca, D., Carminati, E., Doglioni, C., & Marcantoni, D. (2007). Slab retreat and active shortening along the Central-Northern Apennines. In O. Lacombe, J. Lavé, F. Roure, & J. Verges (Eds.), *Thrust belts and Foreland Basins: From fold kinematics to hydrocarbon systems*. *Frontiers in Earth Sciences* (pp. 471–487). Berlin: Springer.
- SeisImager. (2009). *Windows software for analysis of surface waves. SWTM Manual*. California: Geometrics, Inc.
- SESAME European project. (2004). *Site Effects Assessment using Ambient Excitations; Deliverable D23.12: Guidelines for the implementation of the HV spectral ratio technique on ambient vibrations: Measurements, processing and interpretation; deliverable D13.08*. Final report WP08, Nature of noise wavefield.
- Tarabusi, G., & Caputo, R. (2016). The use of HVSR measurements for investigating buried tectonic structures: The Mirandola anticline, northern Italy, as a case study. *International Journal of Earth Sciences*, *106*, 341–353. <https://doi.org/10.1007/s00531-016-1322-3>.
- Team, Geo Mol. (2015). *GeoMol—Assessing subsurface potentials of the Alpine Foreland Basins for sustainable planning and use of natural resources—Project Report* (p. 188). LfU: Augsburg.
- Thorson, J. R., & Claerbout, J. F. (1985). Velocity-stack and slant-stack stochastic inversion. *Geophysics*, *50*, 2727–2741.
- Tsai, N. C., & Housner, G. W. (1970). Calculation of surface motions of a layered half-space. *Bulletin of the Seismological Society of America*, *60*, 1625–1651.
- Vannoli, P., Burrato, P., & Valensise, G. (2014). The seismotectonics of the Po Plain (Northern Italy): Tectonic diversity in a blind faulting domain. *Pure and Applied Geophysics*, *172*, 1105–1142. <https://doi.org/10.1007/s00024-014-0873-0>.